DEGREE PROJECT IN MATERIALS SCIENCE AND ENGINEERING, SECOND CYCLE, 30 CREDITS

STOCKHOLM, SWEDEN 2020

Characterization of Secondary Carbides in Low-Alloyed Martensitic Model Alloy Tool Steels

JUBICA

KTH ROYAL INSTITUTE OF TECHNOLOGY
SCHOOL OF INDUSTRIAL ENGINEERING AND MANAGEMENT

ABSTRACT

The development of tool steels for making and shaping other materials requires a better understanding of the material's properties during manufacture. These high-quality steels include many alloying elements, which give increased hardness during tempering. For producing hardened microstructures, austenite generation is essential. The martensite formed by rapid quenching of austenite followed by tempering helps develop high strength steels. Studying carbide precipitation is a challenge as they are very small in size, present only in small volume fractions and high number densities. The carbide reactions are complicated due to so-called metastable carbides, which are only present as part of the precipitation process. This work focuses on model alloys with two main elements in addition to iron and carbon, molybdenum, and vanadium, to clarify and simplify the carbide characterization. This is done to determine the effect of molybdenum and vanadium carbides on the overall hardness. In this work, two model alloys, A and B, are tempered at 550°C and 600°C with the same vanadium content but different molybdenum contents. The hardness of the materials is evaluated and compared at these temperatures. A more detailed characterization work is done for material A with Scanning Transmission Electron Microscopy-Energy Dispersive Spectroscopy (STEM-EDS) to understand the microstructure and analyze the precipitates. Simulations are performed with Thermo-Calc Prisma (TC-Prisma) to support the experimental work, which includes the simulation of the secondary carbide precipitation, mainly molybdenum carbides in material A tempered for 24h at 600°C, and predicts the carbide precipitation behavior in this steel. The results from STEM-EDS and TC-Prisma for material A, show that the small secondary carbides in the martensite contribute to the increased strength of material A. Due to the overaging of the carbides at 600°C, the hardness at 550°C is higher than at 600°C for material A. The given thesis work is an attempt to interpret the development of secondary carbides of Mo and V in the martensitic matrix and their role in the overall hardness.

Keywords: martensitic steel, secondary hardening, precipitation, STEM, EDS, Prisma, size distribution

SAMMANFATTNING

Den ständiga utvecklingen av högpresterande stål för transport, konstruktion och energisektorn kräver bättre förståelse för materialets egenskaper vid tillverkning. Dessa martensitiska stål inkluderar många legeringselement vilket ger ökad hårdhet vid härdning och anlöpning. Att studera utskiljning av karbider är en utmaning eftersom de är närvarande endast i liten volymsfraktion. Karbidreaktionerna är komplexa till följd av så kallade metastabila karbider vilka endast är närvarande vid en del av utskiljningsförloppet. För att tydliggöra och förenkla karbidkarakteriseringen fokuserar detta arbete på modellegeringar med två huvudelement utöver järn och kol, molybden och vanadin. Detta görs för att fastställa effekten av molybden och vanadinkarbider på den totala hårdheten. I detta arbete studeras två modellegeringar, A och B, härdade och anlöpta vid 550 °C och 600 °C med samma vanadininnehåll men olika molybdeninnehåll. Materialens hårdhet utvärderas och jämförs vid dessa temperaturer. Ett mer detaljerat karaktäriseringsarbete görs för material A med hjälp av STEM-EDS för att förstå mikrostrukturen och analysera utskiljningarna. Simuleringar görs med TC-PRISMA för att stödja det experimentella arbetet, vilket inkluderar simulering av den sekundära karbidutskiljningen och predikterar karbidstrukturen i dessa stål. Resultaten visar att de små sekundärkarbiderna i martensiten bidrar till den ökade styrkan hos material A. Hårdheten vid 550 °C är högre än vid 600 °C för material A eftersom både utskiljningen av karbider är sker långsammare och även dislokationsåterhämtning.

Nyckelord: martensitiskt stål, sekundärhärdning, utskiljning, STEM, EDS, PRISMA, storleksfördelning

LIST OF ABBREVIATIONS

bcc	body centered cubic
bct	body centered tetragonal
BF	Bright Field
DF	Dark Field
EDS	Energy Dispersive Spectroscopy
fcc	face centered cubic
h	Hour
hcp	hexagonal close packed
HV	Vickers Hardness
kgf	kilogram force
KWN	Kampmann-Wagner numerical
LOM	Light Optical Microscopy
LS	Langer-Schwartz
Ms	Martensitic start temperature
Mf	Martensitic finish temperature
PDF	Probability Density Function
PSD	Particle Size Distribution
SEM	Scanning Electron Microscopy
STEM	Scanning Transmission Electron Microscopy
TC-Prisma	Thermo-Calc Prisma Module
TEM	Transmission Electron Microscopy

LIST OF SYMBOLS

ε	Epsilon
μ	Mean
σ	standard deviation
x	random variable
Π	Pi
J(t)	Nucleation rate
J_s	steady state nucleation rate
τ	incubation time
t	Isothermal reaction time
Z	Zeldovich factor
β^*	atomic or molecular attachment rate
N_0	number of available nucleation sites per unit volume
ΔG^*	Gibbs energy of formation
k	Boltzmann's constant
T	Absolute temperature
β	second phase
α	Matrix
$\Delta G_m^{\alpha \to \beta}$	Maximum driving force for precipitation of β from α
Θ	a constant
X_i^{β}	Critical composition from the α matrix
σ'	Interfacial energy
V_m^{β}	molar volume of β
r*	critical radius
a	Lattice parameter
D_i	diffusion coefficient in the matrix
n	components in flux-balance equations
v	growth rate
c_i	volume concentration
Mi	atomic mobility in the matrix
μ'	Chemical potential
r	Particle size
ξ_i	Effective diffusion distance factor
v'	Corrected velocity
$\langle r \rangle$	Mean radius
N_v	Number density

LIST OF FIGURES

LIST OF TABLES

CONTENTS

1 INTRODUCTION

High-quality tool steels are used mainly for working and shaping other materials. The large-scale usage of these steels makes it necessary to design them thoroughly based on the principles of materials engineering. The performance of these steels is related to their properties, which are dictated by the underlying microstructure. Therefore, the micro- and nano-structures play a significant role in determining the bulk properties. The effective control of these structures depends on the alloy composition, processing route, and heat treatment. The development of hardened microstructure in the tool steel requires martensite formation from the austenite by rapid quenching. The tempering of this martensite then results in the formation of high strength steels. Precipitation during tempering of martensitic steels places a challenge in this work. Strong carbide forming elements are added to form nano-sized secondary carbides during tempering, to induce secondary hardening in these steels. This is achieved by alloying with small amounts of vanadium, molybdenum, and other strong carbide formers either individually or in combination to provide an additive effect on the hardness. These alloying elements also have a temperature range in which they are most effective, depending on the alloy composition and the processing parameters [1].

A combination of size ranges from micrometers down to nanometers of these secondary particles is formed during steelmaking until the successive finishing treatments. The fine dispersions of secondary carbides in steels and their low volume fractions make it challenging to analyze and monitor all the different types of carbides precipitated. Thus, it is necessary to study a few carbide types to pinpoint their effect on the properties of the steel. In addition to this, the implementation of high-resolution techniques like STEM and EDS is essential to develop an overview of the type, size, and distribution of these secondary carbides. The effectiveness of these measurements have been shown in many characterization work, for example, quantification of the precipitate size distribution of MoC and Ti(C,N) as a consequence of laser welding [2], precipitation studies of niobium carbides [3], nucleation, growth and coarsening studies of $M_{23}C_6$, NbC, and V(C,N) precipitates [4], precipitation studies of hot-work tool steels [5], and, precipitation studies of secondary carbides for commercial low-alloy steels [6].

The precursor to my work is the study of a commercial tool steel [6], in which the steels were tempered at 550ºC and 600ºC. Tempering led to the precipitation of cementite and other secondary carbides. The presence of silicon restricted the growth of cementite due to which the cementite particles were in the same size range as the secondary carbides. This posed to be a hindrance in the characterization of these steels since the presence of small cementite particles made it difficult to conclude the hardness contribution from the secondary carbides only. Thus, to address this limitation, simplified composition leading to model alloy tool steels with more controlled heat treatment is studied. The investigated steels have two major elements, vanadium, and molybdenum where other elements (Si, Mn, P, S, Cr, Ni, Ti, Nb, Cu, Co, N, Sn, W, Al, Ta, Ca, B) are present in trace amounts. The simplified composition as compared to the commercial steel, derives the name of the model alloy in this work. This indicates that few types of particles are formed compared to that of commercial alloys [6] during processing. Generally, removing primary carbides from the material by austenization at higher temperatures ensures increased precipitation of the secondary carbides during the tempering stages due to more solutes in

solution [7]. In other words, high-temperature austenization promotes a more significant dissolution of the alloying carbides and greater supersaturation of the alloying elements in the martensite, that are available for an intense secondary hardening during tempering [8]. However, in the present work on the model alloy steels, not all the primary carbides could be entirely removed by austenization at 950°C and were present in the martensitic microstructure.

This work aims to study the precipitation of secondary carbides, mainly vanadium carbides and molybdenum carbides, during the tempering of as-quenched martensite at different tempering times and temperatures. The steel is micro-alloyed with vanadium and molybdenum, having a carbon content of about 0.3%. The secondary carbides are crucial to the high strength of these steels and hence are essential to study. Their size range varies between 1 to 10 nanometers in diameter. The research question of this thesis project can thus be formulated as:

What happens to these carbides at 550°C and 600°C and longer tempering times? How do the carbides evolve in terms of particle size during the heat treatment? How do these secondary carbides affect the hardness, and when is the hardness peak reached?

The report is structured in the following way. Section 2 consists of the background information about the literature study required for this thesis work; section 3 presents the materials studied, the experimental methods with the sample preparation techniques, and the simulation parameters used in TC-Prisma; section 4 includes the results obtained from the different experimental methods and the precipitation modelling using TC-Prisma; section 5 provides explanation of the ongoing processes, the reasons behind them, the similarity between experimental and modeling results, the comparison between commercial alloy tool steels and model alloy tool steels and discusses about the environmental, ethical and social aspects related to this work ; section 6 concludes the work by highlighting the important inferences from this study and section 7 recommends the future studies that can be done as a long term goal.

2 BACKGROUND

2.1 MARTENSITE AND MARTENSITIC TRANSFORMATION

The martensitic phase in the iron-carbon system is the result of the rapid quenching of high-temperature austenite. The transformation is essentially diffusionless as negligible time is available for the carbon atoms to diffuse into new lattice sites. Lattice displacement [9] happens when the face-centered cubic (fcc) solid solution of austenite is quenched at a fast cooling rate. This prevents the diffusional decomposition above the martensitic temperature range. Thus, a supersaturated fcc austenite with interstitial carbon atoms that have undergone sufficiently large strains during quenching produces a body-centered tetragonal (bct) structure, which is termed as martensite. Hence, the martensitic transformation is diffusionless, lattice displacive, and shear-induced [10] [11].

2.2 UNTEMPERED MARTENSITE

Untempered martensite is the pure martensite in which different tempering processes take place. In steels, austenite always has the fcc structure, but the martensite formed may have bcc, bct, or a hexagonal close-packed (hcp) crystal structure. The term martensite has been used invariably for all steel compositions. The crystal structure depends on the carbon content, and there are considerable changes in the microstructures and crystallography of different steel types. For a tetragonal structure of martensite, the c/a ratio can be estimated by the formula 1.005 + 0.045(wt% C), as described in [12]. In the untempered martensite, the substitutional elements remain dissolved in the matrix similarly as that in the austenite phase at higher temperatures. It can be inferred that the composition of the untempered martensite is similar to that of the austenite prior to the transformation [11] [12].

Figure 1 shows the martensitic start temperature (Ms) and the martensitic finish temperature (Mf) for the variation in the carbon content up to 2%. It also depicts the transition in the martensite structures from lath to plate at increasing carbon content.

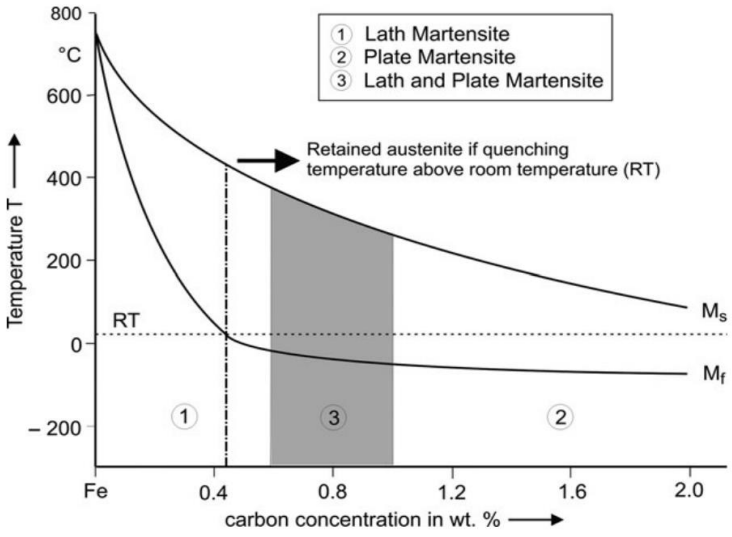

Figure 1 Influence of carbon content on the martensitic structure [13].

2.3 AUTO TEMPERING

It is known that most of the steels have a Ms above room temperature [14]. The Ms depends on the carbon content in steels inversely, i.e., Ms decreases when carbon content increases, as well as on the alloying elements. The martensite formation during quenching requires enough undercooling to initiate the transformation. Once the energy barrier is overcome, the transformation starts instantly. The martensite that forms near the Ms gets time to temper until the quenching process is over. This event is said to be auto tempering or quench tempering [15]. The carbon atoms in the initial martensite then undergo redistribution to lower energy sites [14].

Auto tempering can have several forms. The carbon atoms are segregated in two ways [16]:

- Segregation of the carbon atoms to dislocation sites: The martensitic transformation is usually accompanied by the formation of a large number of dislocations. For a steel with 0.2% carbon, the dislocation density in the martensitic state is reported to be in the range 0.3 and 1.0 x 10^{16} m^{-2} [14][15]. The dislocations provide lower energy sites than the interstitial sites. Hence, the carbon atoms are redistributed to these sites. This is said to be carbon segregation, which does not involve carbide precipitation.

- Segregation of carbon atoms to interlath austenite films: The carbon atoms can also be redistributed at the austenite/martensite interface during quenching. The steels that have high Ms and medium carbon content depict this situation of carbon segregation. Consequently, there is an enrichment of carbon atoms at the interlath austenitic films.

2.4 HEAT TREATMENT

Heat treatment is usually done for the steels to enhance the material properties. This section gives a basic introduction of the mechanisms taking place during the tempering process for low-alloyed steels. Martensite in the as-quenched state is very hard and brittle. Tempering the as-quenched martensite helps to reduce the brittleness. Tempering usually results in the precipitation of carbides that eventually balance hardness and ductility. During tempering, four mechanisms are active and are generally coinciding.

- Stage 1 (dominant up to 250ºC): The precipitation of ε carbide takes place in the martensite. The chemical composition of ε carbide is $Fe_{2.3}C$ with an hcp structure. The presence of ε carbide depends on the carbon content of the steel. For carbon content more than 0.2 wt%, the ε carbides are first to precipitate after the above-mentioned segregation. However, in low carbon steels, negligible ε carbide is reported [12]. This is because the carbon atoms tend towards the lower energy dislocation sites and hence are unavailable for precipitation. It is noted that at the end of stage 1, there is a partial loss in the tetragonality of martensite due to the precipitation of ε carbide [15].

- Stage 2 (dominant between 200ºC and 300ºC): The main course of action in this stage is the decomposition of retained austenite [14] [17]. The amount of retained austenite depends on the carbon content. As the carbon content increases, the amount of retained austenite increases. The retained austenite decomposes into bainitic ferrite and cementite [15].

- Stage 3 (dominant between 200ºC and 350ºC): The transition carbides, including ε carbide, are replaced by cementite. The cementite can nucleate at the ε carbide interfaces with the matrix, twins in higher carbon martensite, lath martensite boundaries, or prior austenite grain boundaries. At the ε carbide interfaces with the matrix, as the cementite particles grow, the ε carbide particles disappear. The atomic arrangement of the iron atoms at the twin boundaries is similar to that in the cementite, and hence cementite can grow at these twins. At this stage of tempering, the tetragonality of martensite disappears. The structure then consists of ferrite that is not supersaturated with carbon [15].

- Stage 4 (dominant above 350ºC): At this stage, the coarsening of cementite takes place by Ostwald ripening, where larger particles grow at the expense of the smaller particles. The coarsening starts between 300ºC and 400ºC. Further increase in temperature (up to 700ºC) leads to the spheroidization of cementite particles that initially had needle-like morphology in martensite [15].The nucleation and growth of the secondary carbides start at an early stage where the diffusivities of the substitutional elements are sufficient. This leads to the precipitation of secondary carbides in which the alloying elements like Ti, Mo, V form carbides. These secondary precipitates increase the hardness of steels by replacing the cementite that has a coarser structure by fine alloy carbides such as TiC, V_4C_3, and Mo_2C [14].

2.5 ALLOYING ELEMENTS AND TEMPERING

The addition of alloying elements generally alters the thermodynamics and the kinetics of the austenite to martensite transformation. The most obvious modifications are in the suppression of the martensitic start and finish temperatures and the shift of the time-temperature-transformation curves towards longer times. Other alterations include stabilization of the ε carbides in the martensite, retention of the tetragonal lattice even after tempering, retention of austenite after quenching, resistance to softening during tempering, and prevention of the coarsening of cementite [15][18]. A good combination of alloying elements along with the cooling rates to obtain a fully martensitic structure is one of the ways to design steel with high hardness and toughness. It is important to note that the temperature ranges in which the metastable carbides form, the decomposition of retained austenite takes place, cementite forms, and the secondary carbides precipitate is a function of the alloy composition and the tempering conditions.

In general, the behavior of the alloying elements during tempering of the steels can be summarized as follows:

- **Molybdenum**: It is a strong carbide former that resists the softening during tempering. At higher temperatures, molybdenum partitions to the carbide phase and keeps the carbide particles small and numerous [19]. Figure 2 validates the effect of molybdenum on hardenability through the hardenability multiplying factor. When molybdenum is present in the solid solution in steels, it reduces the carbon diffusivity. This reduction stabilizes the austenite and prevents the formation of ferrite and pearlite during quenching. Thus, molybdenum shifts the time-temperature-transformation curves towards the right [20].

- **Vanadium**: It is a stronger carbide former than molybdenum and chromium. At the similar composition levels as molybdenum and chromium, vanadium has a much more potent effect [21]. Vanadium forms alloy carbides at higher tempering temperatures that replace coarser carbides, like cementite, thereby retarding the coalescence and the coarsening [19]. Vanadium limits grain growth and also resists the softening during tempering [18].

- **Silicon**: The presence of silicon inhibits the conversion of ε carbide to cementite. This occurs during the tempering of martensite in the temperature range from 100ºC-300ºC. Silicon takes time to diffuse in the carbide due to its inability to dissolve in it that nearly halts the migration of carbon atoms to and from the particles. This helps in retarding the softening of the steels during tempering [14][19][22]. The kinetics of martensitic recovery is influenced by the silicon content. A reduction in the dislocation cross slip occurs when silicon is present in bcc iron. An increase in free energy takes place in the ferrite lattice due to Si-Si interaction. This interaction raises the stress for the dislocation movement and hence lowers the recovery [23]. Silicon increases the hardness of tempered martensite by solid solution hardening [1].

- **Manganese:** Manganese influences the size of the secondary carbides by preventing them from coalescing, thus increasing the strength. The presence of manganese in the ferrite matrix leads to the increase in the number density of smaller carbides and offers a lower state of recovery in the martensite. This leads to an increase in the hardness of tempered martensite [1] [19].

- **Chromium:** The tempering of martensite is hindered by chromium at all tempering temperatures. A delay in the softening process is seen in the presence of chromium [19] [22]. However, rapid coarsening of chromium carbides, Cr_7C_3 takes place around 550ºC to 600ºC due to the fast diffusion of chromium in the ferrite matrix [24]. This provides little or no secondary hardening as compared to more stable carbides like Mo_2C [14].

- **Nickel**: The solubility of carbon in the martensitic matrix is decreased by nickel that remains in the solid solution during tempering. This provides a more significant supersaturation effect by which the higher carbon content in the matrix promotes the formation of alloyed carbides. This leads to an enhanced secondary hardening process [19][25].

2.6 HARDENABILITY OF STEELS

The elements like molybdenum, manganese, chromium, copper, and nickel boost the hardenability by delaying the time required for the austenite decomposition into ferrite and pearlite. This can be done either by reducing the growth rate or the nucleation rate of ferrite, pearlite or bainite [26]. Hardenability is influenced by the austenite grain size and the chemical composition of steels. As the austenite grain size increases, the grain boundary area per unit volume decreases. This reduces the number of nucleation sites for ferrite and pearlite. Therefore, the transformations slow down, and the tendency to form these structures decreases, thereby increasing the hardenability[27]. Figure 3 shows the base hardenability as a function of the austenite grain size. Base hardenability is the hardenability of steel that comes from the carbon content. For a strong carbide forming element like molybdenum and vanadium, the growth rate

of pearlite is reduced by the solute drag effect [26][27]. This effect depicts the state when the solute atoms prevent the motion of grain boundaries [13].

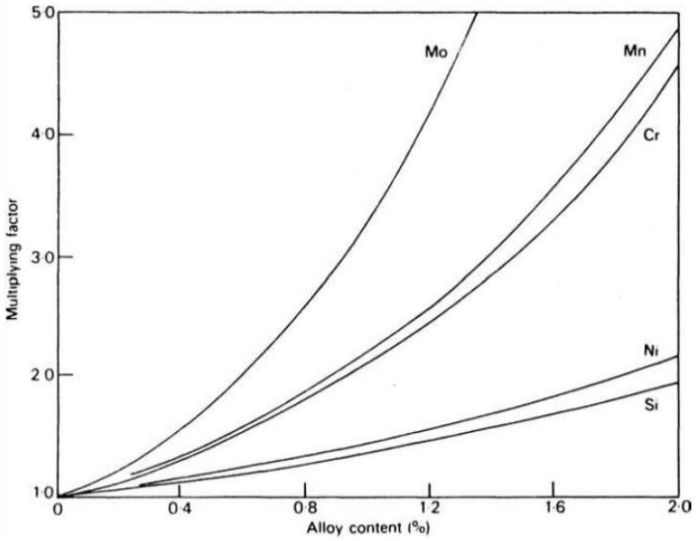

Figure 2 Variation of alloy content with hardenability multiplying factor[28].

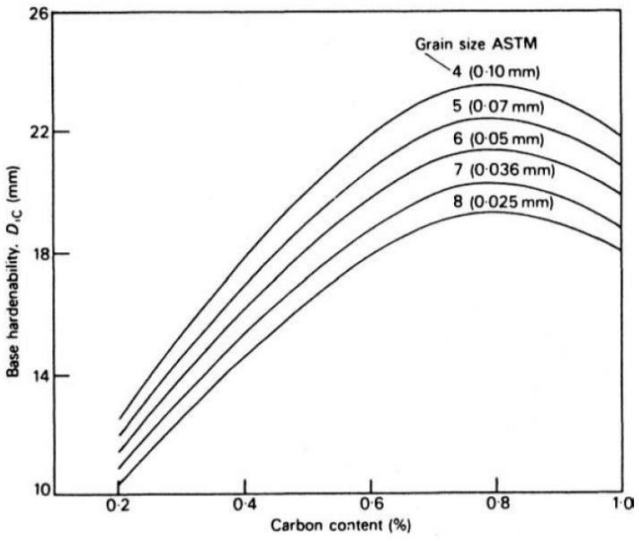

Figure 3 Base hardenability as a function of the austenite grain size [16].

2.7 SECONDARY HARDENING

The hardness of martensite in the as-quenched state depends mainly on the carbon content. When the as-quenched low alloyed martensite is tempered, the hardness decreases [1]. Figure 4 depicts the hardness as a function of carbon content in the as-quenched martensitic state. The presence of strong carbide formers like chromium, molybdenum, vanadium, tungsten results in the precipitation of carbides when tempered in the temperature range between 500ºC and 600ºC. This is known as precipitation strengthening. The substitutional diffusion of these alloying

elements in contrast to the interstitial diffusion of carbon and iron depend on the combined effect of the availability and the diffusivity of the participating elements. The carbide formation by the micro-alloying elements is a slow process when compared to the diffusion of carbon and iron. This results in a finer dispersion of the carbides due to their larger atomic radii in the iron matrix, causing lesser diffusion distance when compared to the carbon atom. These carbides are resistant to coarsening at higher temperatures thereby increasing the toughness [29]. The dissolution of the coarse cementite particles and their replacement with fine alloy carbides dispersion lead to an increase in toughness [21]. However, this is true for short tempering times in which both hardness and toughness increase. At long tempering times, the toughness increases, but the hardness decreases due to the coarsening of carbides [14].

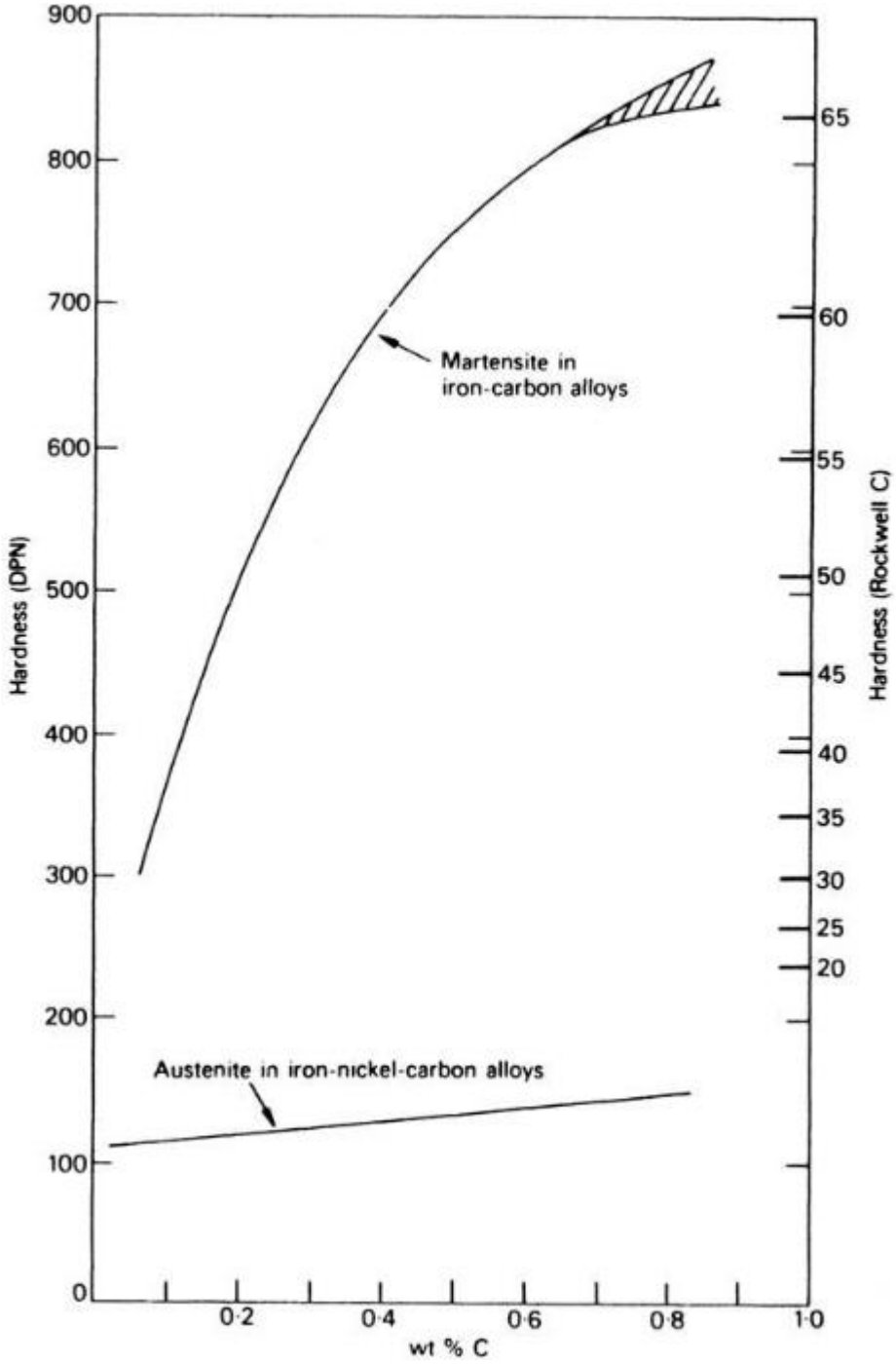

Figure 4 Effect of carbon content on hardness [30].

Molybdenum plays a crucial role in increasing the hardness of martensitic steels. It forms fine dispersions of carbides at the dislocations present in the as-quenched martensite. A clear picture of the stability of the molybdenum carbides can be obtained from the Thermo-Calc equilibrium phase calculations. In this exercise, the focus is to find the stable phases of molybdenum in the Fe-C-Mo system and Fe-C-Mo-V system by varying the amount of molybdenum and the temperature. The mass percent of carbon used is 0.339%, and molybdenum is varied from 0-

10%, where attention is given at 2%, and 8% for the low and high content of molybdenum, respectively. In the Fe-C-Mo-V system, the vanadium is 0.14%. The temperature was varied from 100ºC-1000ºC. The alloy composition and temperature are selected to match the experimental conditions of this work, described later in the report. From this set-up, the equilibrium phase diagrams of the Fe-C-Mo system and Fe-C-Mo-V system were obtained, Figure 5 and Figure 6. These show the phases of molybdenum carbide with different crystal structures corresponding to the varying conditions of the system.

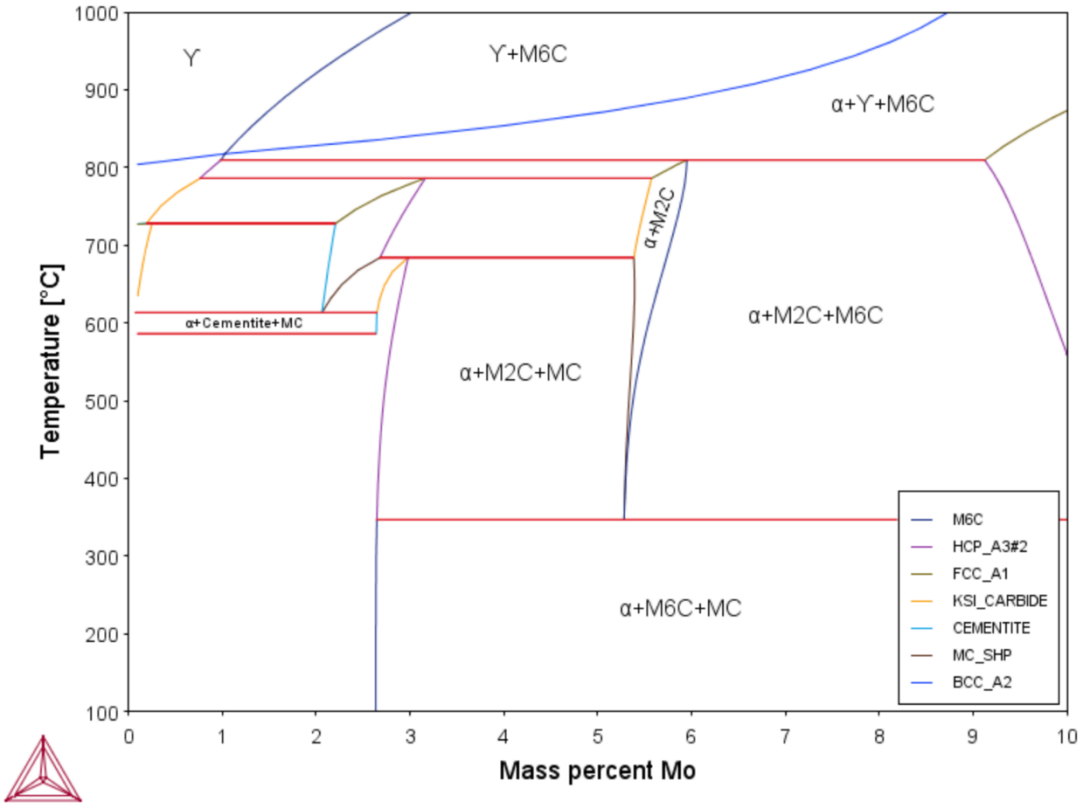

Figure 5 Thermo-Calc equilibrium phase diagram of Fe-C-Mo alloy system, α: Ferrite, Y: Austenite.

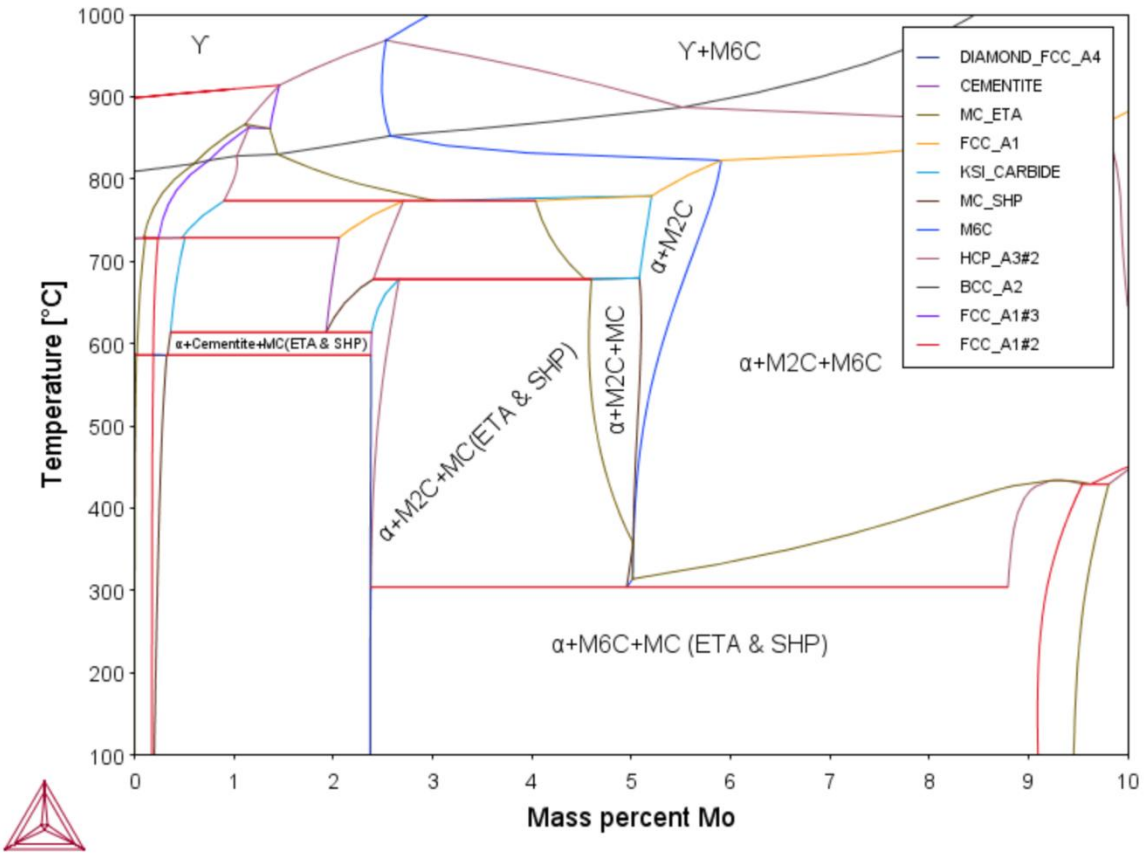

Figure 6 Thermo-Calc equilibrium phase diagram of Fe-C-Mo-V alloy system, α: Ferrite, Y: Austenite.

The tempering of steels leads to the formation of different types of carbides of molybdenum and vanadium. With the increasing molybdenum content in the steels and varying temperatures, the stability of the carbides also varies. Some are metastable carbides and are only present in the course of the precipitation process and some are stable carbides present in a considerable temperature range. Figure 5 and Figure 6 explain the carbides that are forming as a function of the amount of molybdenum and the temperature. The focus is on the phases forming at 600°C for the varying composition of molybdenum. From the single equilibrium calculation, the phases present at low and high molybdenum contents are given in Table 1 and Table 2 as follows:

Table 1 Phases present when the temperature is 600°C in the Fe-C-Mo system

Low content, Mo = 2 mass%	High content, Mo = 8 mass%
Phases are: Ferrite and MC	Phases are: Ferrite, M_2C and M_6C

Table 2 Phases present when the temperature is 600°C in the Fe-C-Mo-V system

Low content, Mo = 2 mass%	High content, Mo = 8 mass%
Phases are: Ferrite, cementite and MC (SHP & ETA)	Phases are: Ferrite, M_2C and M_6C

From the exercise above, the concentration of molybdenum and vanadium in the matrix and the tempering conditions affect the sequence of the precipitation of their carbides and their stability.

2.8 ELECTRON MICROSCOPY

2.8.1 STEM

STEM combines the principles of Transmission Electron Microscopy (TEM) and Scanning Electron Microscopy (SEM). It has the ability of atomic-resolution imaging and nanoscale analysis. Like TEM, STEM requires very thin samples that are in the nanometer scale. TEM and STEM are related by Helmholtz reciprocity [31]. A STEM is essentially a TEM with the positions of the electron source and point of observation switched relative to the direction of travel of the electron beam, Figure 7. The optical arrangement of the STEM is the same as a TEM, but the operation is modified by flipping the direction of the travel of the electrons. In STEM, various detectors with collection angles are present that can be adjusted depending on the desired electrons to be captured, whereas, in TEM, the aperture is used to control the electrons to be detected [31].

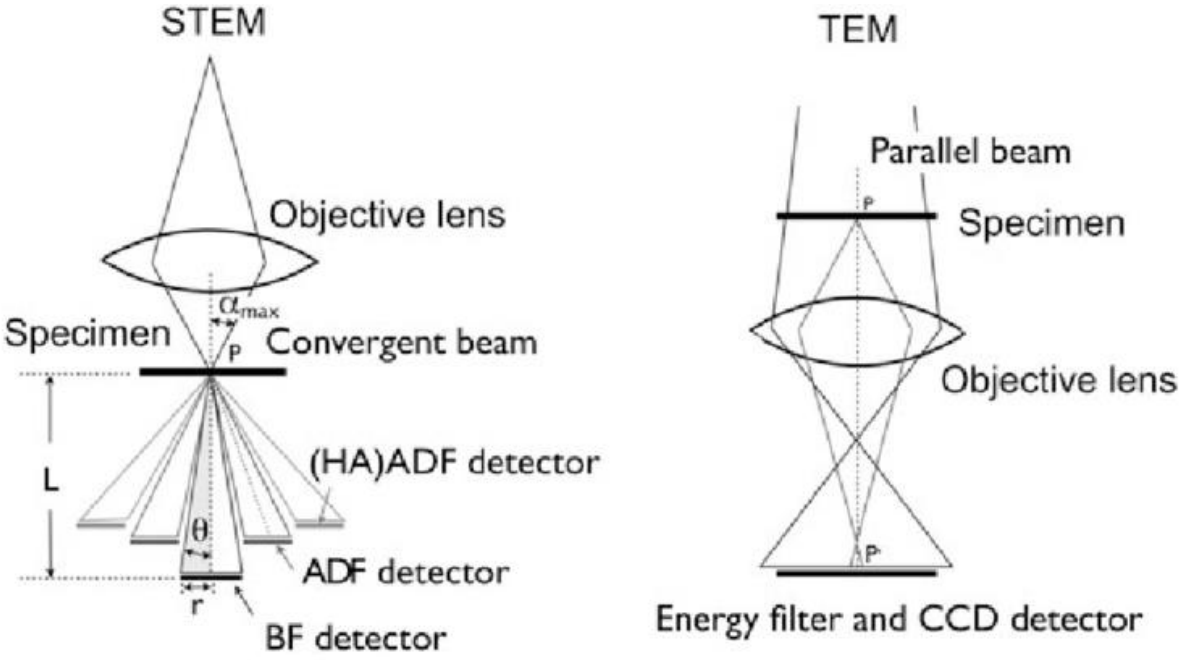

Figure 7 Orientation of TEM and STEM [32].

In addition to the similarity with TEM, STEM also shares similarities with the SEM. A beam of electrons generated by an electron gun is focused by a series of electromagnetic lenses to form an image of the electron source at the specimen. The lens system provides the demagnification of electron beams to form an atomic scale probe at the sample. This electron spot, or probe, is scanned over the sample in a raster pattern by exciting scanning deflection coils. The electrons that are scattered are detected, and their intensity is plotted as a function of probe position to form an image. Since STEM uses a focused beam, scattering in the sample gives a convergent beam electron diffraction pattern [33]. Compared to SEM that uses a bulk sample, the STEM demands a thin, electron-transparent specimen that must be less than 100 nm in thickness.

Therefore, the STEM detectors are placed after the sample and detect the transmitted electrons. The probe spreading within the sample is relatively small as a thin sample is used, and the size of the probe controls the spatial resolution of the STEM. Thus, the crucial image-forming optics are those before the sample that form the probe.

In TEM, the chromatic aberrations are pronounced due to varying electron energies being focused at different focal positions. The thicker the foils in the lens are, the more chromatic aberrations will be. As in TEM, the lenses are after the sample, and these aberrations are more than in STEM. Another advantage of STEM over TEM is that the signals that cannot be spatially correlated in TEM can be done in STEM, including secondary electrons, scattered beam electrons, characteristic X-rays, and electron energy loss. This indicates that the spatial resolution can be very high based on the incident probe size, and the image contrast can be directly interpreted [34]. Hence, STEM can be concluded as a very powerful and highly versatile instrument.

2.8.2 EDS

EDS is an analytical technique used for the elemental analysis or chemical characterization of a sample or a sample surface. It can be used both for qualitative analysis and quantitative analysis. A beam of high energy charged particles; usually, electrons or protons, or a focused X-ray excites the electronic structure of an atom when the surface is irradiated by the beam. This causes the ejection of electrons from inner atomic shells that are filled with electrons from the outer atomic shell. This electron transition from higher energy levels to lower energy produces an X-ray. X-ray emission is characteristic of each element, and hence a “fingerprint” or “signature” spectrum obtained via this method can be used for identification of the element upon comparison with a reference spectrum [35]. The identification of the signature spectrum of an element is the qualitative analysis, whereas quantitative analysis determines the concentration of the elements, which is measured by the intensities of the peaks [36].

There are four primary components in an EDS apparatus: the excitative source (electron beam or X-ray beam), the X-ray detector, the pulse processor, and the analyzer. An excitatory electron beam is used in electron microscopes, SEM, and STEM. The conversion of X-ray energy into voltage signals is done by the detector; the voltage signals are sent to the pulse processor, which measures the signals and passes them onto an analyzer for data display and analysis [37]. The number and energy of these X-rays at each energy level is calculated by the silicon drift detector. The characteristic energy level of each element is the qualitative result, while the frequency of the X-rays with this energy level is the quantitative result. The frequency of the X-rays or the count of X-rays versus the energy level of the X-rays is presented by a typical spectrum. Automatic detection and quantification of the elements in the sample are possible by new EDS systems that come pre-calibrated. The interaction volume in the sample from which X-rays are emitted is in the shape of a teardrop beneath the surface. This volume size is defined by the accelerating voltage used and the density of the material. The X-rays can be generated from any electron transition shells, K, L, or M, depending on the extent of the excitation available. Often wrong elements may be detected when overlapping of the energy levels emitted from different elements occurs. Therefore, one has to be cautious while interpreting the EDS results [38].

EDS analysis helps to determine the elemental composition of individual points or to map out the lateral distribution of elements (spatial variation of elements) from the imaged area. The lateral distribution of the elements is obtained when the electron beam is swept over an area of the sample [39]. It can also be used to obtain compositional information on larger specimens (low SEM magnification, high accelerating voltage) or on specific particles, morphologies, or isolated areas on filters or within deposits. The EDS has an analytical capability that can be coupled with several applications, including SEM, TEM, and STEM [40].

2.9 LOG-NORMAL SIZE DISTRIBUTION

The size distribution of precipitated particles can be best understood by a particle size distribution depicted in a graphical format. The common idea is to divide the data of the size of particles into a number of discrete size classes. A histogram of this grouped data can thus show how the sizes of the particles are distributed across different size ranges. To get standardized data with respect to the interval size, the number of particles is divided into each interval by the size of that interval. For a more generalized data handling and to avoid ambiguity in the amount of data collected for the different samples in the microscopy investigations, normalized size distribution is followed. This is done by dividing the number of particles in each size interval by the total number of particles observed in that sample. This normalized histogram is a step-like portrayal of the particle size distribution function, which is the Probability Density Function (PDF) [41]. A PDF helps in specifying the probability where a random variable is most likely to fall within a given range of values. This probability lies within the area under the density function. Mathematically, the area is the integral of the PDF that covers the entire range of the values. The PDF has positive values, and integrating over the entire space gives the value 1 [42]. The log-normal distribution is based on PDF. A log-normal distribution, f(x) of a variable x, ($0<x<\infty$) can be defined as the normal distribution of lnx, i.e., the probability of having x in the interval x, x+dx is f(x)dx with $f(x)=\frac{\boldsymbol{p(lnx)}}{\boldsymbol{x}}$ [43]. If log(x) is normally distributed, then the variable x has a log-normal distribution. The PDF for the log-normal distribution is given by:

$$p(x) = \frac{1}{\sigma x\sqrt{2\Pi}} e^{\left(-\frac{(\ln(x)-\mu)^2}{2\sigma^2}\right)}$$

where, μ is the mean, and σ is the standard deviation of the normally distributed logarithm of the variable x [44].

In the typical bell curve or Gaussian or normal distributions, a small probability of assigning negative values to the distributions exists. This cannot be applied to the variables that can only have positive values like the size of particles [45]. As log-normal distribution is based on PDF that takes only positive values, therefore this type of distribution assures that only positive values are presented. From [44], '*There is also a theoretical justification for using the log-normal distribution: whereas the well-known central limit theorem, in its classical form, says that the addition of many random "effects" has approximately Gaussian distribution, the less well-known version ascertains that the multiplication of many positive random variables creates a distribution that is approximately log-normal. Note that multiplication plays a much more dominant role in natural laws than addition. Since a logarithmic transformation brings log-normal data back to normal and converts multiplication to addition, the renowned statistician John W. Tukey suggested that all "amount" data should be converted to logarithms first. One can then confidently use techniques assuming normal distributions and additive effects, such as*

linear regression and analysis of variance, before returning to the original scale using back-transformation to express and interpret results.' Thus, log-normal distribution results from effects that are multiplicative. This gives the reason to apply this distribution for describing the particle size of the precipitates that grow at their own rate at preferable nucleation sites. When broader particle size distributions are present, log-normal distribution often holds good. A more intuitive realization can be when the particle sizes are present at large intervals, the log-normal distribution tries to bridge this gap and provide a possibility of finding a particle in a given size range. This distribution is symmetrical around the mean on a logarithmic size scale, and the width of the distribution is given by the standard deviation [46].

2.10 MODELING

For the modeling of the precipitation of the secondary carbides, TC-Prisma was used [47]. The software is a general tool for the computation of the diffusion-controlled multi-particle and precipitation processes in multicomponent alloy systems. The nucleation, growth, dissolution, and coarsening of particles are treated as a continuous process in any heat treatment condition. These processes are simulated using Langer-Schwartz (LS) and the Kampmann-Wagner Numerical (KWN) approach in multi-component and multi-phase systems [47]. The KWN approach is an extension of the LS theory. In this approach, during the entire precipitation process, the temporal evolution of the mean radius and particle density is predicted by solving a set of rate equations. These equations are derived with certain assumptions for the rates of nucleation and growth, as well as the PSD [48].

Precipitation involves the development of a second phase particle from the matrix phase and is usually driven by the thermodynamics of the process. The thermodynamics and the kinetics of the bulk and the interface play a crucial role in the formation of the precipitates. The TC-Prisma software is integrated into both the Thermo-Calc and the DICTRA software. The Thermo-Calc database provides the thermodynamic data, whereas the information about the atomic mobility of each element in different phases is provided by the kinetic database, which is included in DICTRA [47]. The data obtained is used for the calculation of the nucleation and the growth rate in the KWN method.

2.10.1 NUCLEATION

The LS theory assumes that the nucleation of new phases occurs as embryos with varied structures or compositions. The time-dependent nucleation rate *J(t)* is expressed as:

$$J(t) = - J_s \exp(-\frac{\tau}{t}) \quad (1)$$

where, J_s is the steady-state nucleation rate, τ is the incubation time for developing feasible nucleation conditions, and t is the isothermal reaction time. The incubation time for an isothermal reaction is given by:

$$\tau = \frac{1}{\theta Z^2 \beta^*} \quad (2)$$

where, Θ is a constant having value 2.

The steady-state nucleation rate can be expressed as:

$$J_s = Z\beta^* N_0 \exp\left(-\frac{\Delta G^*}{kT}\right) \quad (3)$$

where, Z is Zeldovich factor, β^* is the rate at which the atoms or molecules are attached to the critical nucleus, N_0 is the number of available nucleation sites per unit volume, ΔG^* is the Gibbs energy of formation of a critical nucleus, k is Boltzmann's constant, and T is the absolute temperature.

The Gibbs energy of formation for the precipitation of a second phase β from a matrix α is given by:

$$\Delta G^* = \frac{16\pi\sigma'^3}{3(\Delta G_m^{\alpha\to\beta}/V_m^{\beta})^2} \quad (4)$$

where, $\Delta G_m^{\alpha\to\beta}$ is the maximum driving force for precipitation of β from α, which can be obtained by the parallel tangent construction in Thermo-Calc. This is also known as the molar Gibbs energy change for the formation of the β particles with critical composition X_i^{β} from the α matrix. The maximum driving force and the critical composition is obtained by the Newton-Raphson method which is a general calculation technique used in the Thermo-Calc software. σ' is the interfacial energy and V_m^{β} is the molar volume of β.

The success of an embryo to be considered a nucleus formed during the initiation of the precipitation phase is determined by its radius. Nucleation can be understood as a diffusion process in the particle size space. The critical radius of the nucleus is generally accepted as the optimum size for an embryo to be a nucleus. It is given as:

$$r^* = -\frac{2\sigma' V_m^{\beta}}{\Delta G_m^{\alpha\to\beta}} \quad (5)$$

When the radius is slightly higher than the critical radius, the nuclei have the possibility of crossing the energy barrier and precipitate in the matrix. This possibility is measured by Z, Zeldovich factor, and is dependent on the thermodynamics of the nucleation process.

The atomic or molecular attachment rate, β^* depicts the kinetics of the mass transport phenomenon in the nucleation process and is given by:

$$\beta^* = \frac{4\pi r^{*2}}{a^4}\left[\sum_{i=1}^{k}\frac{(X_i^{\beta/\alpha} - X_i^{\alpha/\beta})^2}{X_i^{\alpha/\beta} D_i}\right]^{-1} \quad (6)$$

where, a is the lattice parameter, $X_i^{\beta/\alpha}$ *and* $X_i^{\alpha/\beta}$ are the mole fractions of element i at the interface in the precipitate and matrix, respectively, D_i is the corresponding diffusion coefficient in the matrix [47] [48] [49].

The equations (1) to (6) correspond to homogeneous nucleation but can also be used for heterogeneous nucleation with a difference in the nucleation sites. Homogeneous nucleation takes place in perfect single crystals, whereas heterogeneous nucleation takes place in imperfect crystal or polycrystalline material due to the presence of dislocations, edges, corners, and grain

boundaries. The presence of these imperfections reduces the nucleation barrier, and hence nucleation can take place at a lower driving force.

2.10.2 GROWTH

TC-Prisma provides three different growth models: the advanced model, the simplified model, and the binary dilute solution model. In all these models, a spherical particle of stoichiometric composition or with negligible atomic diffusivity is treated growing under local equilibrium conditions.

The Advanced model is proposed by Chen, Jeppsson, and Ågren (CJA). In the CJA model, the velocity of the interface can be obtained together with the interface concentrations by solving 2n-1 equations numerically. These equations consist of n-1 independent components that comprise the flux-balance equations and the local equilibrium conditions for all n components, i.e.,

$$v(c_i^{\beta/\alpha} - c_i^{\alpha/\beta}) = c_i^{\alpha/\beta} Mi \frac{\mu'^{\alpha}_{i} - \mu'^{\alpha/\beta}_{i}}{\xi_i r} \quad (7)$$

$$\mu'^{\alpha/\beta}_{i} = \mu'^{\beta/\alpha}_{i} + \frac{2\sigma' V_m^{\beta}}{r} \quad (8)$$

where, v is the growth rate, $c_i^{\beta/\alpha}$ and $c_i^{\alpha/\beta}$ are the volume concentrations of component i at the interface in the precipitate and matrix, respectively, Mi is the atomic mobility in the matrix, μ'^{α}_{i} and $\mu'^{\alpha/\beta}_{i}$ are the chemical potentials in the matrix for the average concentration and at the interface, respectively. $\mu_i^{\beta/\alpha}$ is the chemical potential at the interface in the precipitate, r is the particle size, ξ_i is the effective diffusion distance factor, $\frac{2\sigma' V_m^{\beta}}{r}$ is due to the Gibbs-Thomson effect [47] [48] [49].

The effective diffusion distance factor for each independent component is given by

$$\xi_i = \frac{\Omega_i}{2\lambda_i^2} \quad (9)$$

where, $\Omega_i = (c_i^{\alpha} - c_i^{\alpha/\beta})/(c_i^{\beta/\alpha} - c_i^{\alpha/\beta})$ is the dimensionless supersaturation for an individual component, and λ_i is obtained with the following equation:

$$2\lambda_i^2 - 2\lambda_i^3 \sqrt{\pi} \exp(\lambda_i^2) \operatorname{erfc}(\lambda_i) = \Omega_i \quad (10)$$

The solution to the flux balance equations by the CJA model is often time-consuming. Hence, a less rigorous approach through the simplified model is followed to obtain the solution to these equations. By combining the equations (7) and (8), the velocity for the simplified model can be obtained,

$$v = \frac{K}{r}\left[\Delta G_m - \frac{2\sigma' V_m^{\beta}}{r}\right] \quad (11)$$

where, ΔG_m is the driving force, σ' is the interfacial energy, V_m^{β} is the molar volume and K is a factor given by:

$$K = \left[\sum \frac{(X_i^{\beta/\alpha}(r) - X_i^{\alpha/\beta}(r))^2 \xi_i}{X_i^{\alpha/\beta}(r) M_i}\right]^{-1} \quad (12)$$

The interface compositions $X_i^{\beta/\alpha}(r)$ and $X_i^{\alpha/\beta}(r)$ are taken from the tie line across the matrix composition and , ξ_i is the effective diffusion distance factor as stated earlier. [47] [48] [49].

3 METHODOLOGY

3.1 PRECIPITATION SIMULATIONS

Thermo-Calc 2020b was used to perform computational modeling in TC-Prisma that used the thermodynamic database, TCFE7, and the mobility database MOBFE2. The computation was performed in parts. The first part comprised the equilibrium phase calculations for determining the stable phases at equilibrium when the material A was simulated in the temperature range 500ºC to 1000ºC. From the TC, it was seen that all the carbides dissolved in the austenite at temperatures above 900ºC. It was assumed that the composition of austenite and the martensite formed after quenching are the same. Following this calculation, the precipitation calculation was run isothermally for 24 hours at tempering temperature 600ºC. The matrix was assumed to be fully martensitic, having heterogeneous nucleation with a dislocation density of $10^{15}m^{-2}$ in the ferritic matrix for low-carbon martensitic steels [14]. Molar volumes were obtained from the Property Model Calculator. The interfacial energies were taken from three sources; referred from the literature, calculated from TC-Prisma, and modified referring the values from the literature to calculate the mean size that was close to the experimental data. The carbides were assumed to nucleate on the dislocations. The simulations were run for the spherical morphology of the carbides. The simulation mainly focused the molybdenum-rich carbides and the vanadium-rich carbides were not considered for the reasons stated later in the report. The purpose of these simulations was to realize the similarity between the models used in the calculations and the real-life experiments, help explain the processes of the microstructural evolution during tempering, and predict the probable behavior of the material A under modified experimental parameters through simulations.

3.2 EXPERIMENTAL WORK

3.2.1 MATERIALS

The chemical composition of the two model low-alloy tool steels is given in Table 3 and Table 4. At Swerim Kista, the steels were casted, and had undergone homogenization and hot rolling at Swerim Luleå. The chemical composition was measured in D-Lab. Before further austenization and tempering, each of the steel plates was cut into halves, and one halve was saved. The edges of the plates were removed. The plate was then cut into two 1.5 cm width smaller bars. The purpose was to have the same reference as-quenched state for heat treatments at 550°C and 600°C individually. Eight samples, each of 1.5 x 1.5 cm^2, were cut from the as-quenched bars. Hence, a total of 24 samples (including the as-quenched samples) were cut from the plates of material A and B. The samples were austenized at 950ºC for 5 minutes and quenched in water at room temperature. This austenization temperature was chosen from the TC equilibrium calculations, which said that all the carbides dissolved above 900ºC. A high of 50ºC was kept for making sure that none of the carbides remain in the austenitic matrix. After austenization, tempering was done at 550ºC and 600ºC up to 24h with intermediate steps of 0h, 0.5h, 1h, and 4h. Figure 8 depicts this. All of these tempered samples were subsequently quenched in water at room temperature. Here, 0h refers to the as-quenched samples that were taken to tempering temperatures and quenched to room temperature immediately. The temperature profile during the heat treatment was recorded using a logger. One end of the S-type thermocouple was welded to the sample, and the other end was connected to the logger. Thus, the temperature of the surface of the sample was monitored throughout the process. A

fluctuation of ± 5°C was allowed in the temperature. Additionally, for investigating the effect of higher tempering times on material A at 550ºC, tempering was done for 48h, 72h, 96h, and 168h. After the heat treatment of all the samples at the given time and temperatures, the samples were then cut to one-fourth of the depth so that further investigations can be done on the bulk of the initial plate. This was done using a precision cutting instrument with a carbon boron nitride cutting blade. Two of these samples from their respective bars were kept as the reference for as-quenched states. This process was the same for both the steel samples A and B. The sample preparation was done corresponding to the type of specimen required by the intended technique, i.e., optical microscopy, hardness, and electron microscopy.

Table 3 Chemical composition of sample A in weight%

C	Mo	V	Fe
0.339%	1.06%	0.14%	98.29%

Table 4 Chemical composition of sample B in weight%

C	Mo	V	Fe
0.321%	0.79%	0.14%	98.56%

Note: Other elements like Si, Mn, P, S, Cr, Ni, Ti, Nb, Cu, Co, N, Sn, W, Al, Ta, Ca, B, and As are also present in trace amounts in both the samples.

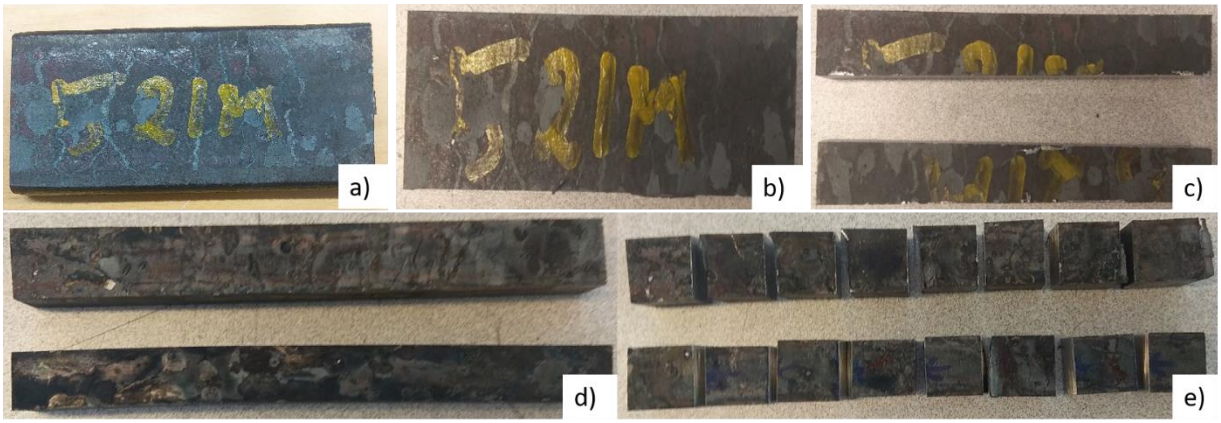

Figure 8 Sample preparation a) Hot rolled plate b) Plate with edges removed c) Plate divided into 2 bars d) Austenized bars at 950ºC for 5 minutes followed by water quenching e) Bars cut into samples.

3.2.2 SAMPLE PREPARATION

3.2.2.1 HARDNESS MEASUREMENTS AND LOM

For characterizing the mechanical property, macro-hardness testing of all the samples was done. This was done to measure the hardness that varied depending on the material, temperature, and time. The instrument used was Vickers hardness tester Qness Q10A+. The load used for indentation was 5 kgf, HV5. The samples for the LOM were prepared by standard metallographic methods and etched in 2% Nital solution.

3.2.2.2 ELECTRON MICROSCOPY

STEM imaging and EDX were performed on the samples that had to again undergo the standard metallographic method as an initial step for producing carbon replicas. The samples were etched with a 2% Nital solution for 5 seconds so that the second phase particles are exposed to the surface. To ensure that the carbon atoms are deposited only on the desired area of the freshly etched sample, the samples were wrapped in aluminum foil, exposing the selected location. After the deposition, the aluminum foil was removed. The deposition was done by carbon sputtering, and an approximately 20 nm thick carbon film was deposited on the surface of the sample. Precision Etching and Coating System (PECS, Gatan), Model 682, was used for this purpose. A fine grid was made on the carbon film using a scalpel. The sample was etched again using 10% Nital. This time it is ensured that the etchant seeps into the material, and hence this is where the grid plays the role. Pipette was used to introduce the etchant in the crevices of the sample through the grid. After a while, air bubbles began to appear over the sample surface. It was observed that small fragments were loosening from the sample that need to be collected on the copper (Cu) grids. Some of the fragments were collected from the etchant, cleaned twice in ethanol and then in water. When in ethanol, the fragments seemed to shrink and stretch when introduced in water. This is due to the surface tension difference between ethanol and water. The properly stretched fragment was then collected on the Cu grid. The diameter of the Cu grid was 3.05 mm having 400 square meshes. The entire process depicts carbon replica extraction and is suitable for our STEM investigations. Figure 9 shows the process in a series of sample stages.

STEM images were obtained from the carbon replica samples of the material A. Bright field (BF), and Dark field (DF) modes were used to acquire the images. The spot size used was 1.5 nm. The camera length in BF mode was 80 cm, and in DF mode was 12 cm. Jeol JEM-2100F Field Emission Electron Microscope was used for this purpose. From the EDS analysis of each point in the carbon replica sample, the atomic% of vanadium, molybdenum, and iron was obtained. Carbon and other elements in trace amounts were excluded from the analysis.

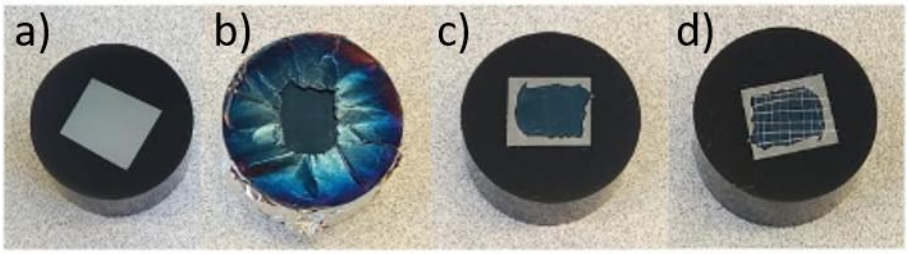

Figure 9 Sample preparation for carbon replica a) Etched with 2% Nital b) Sputtered with carbon c) After removing the aluminum foil d) Fine grid formation on the sputtered part of the sample.

4 RESULTS

4.1 TC-PRISMA

The phase equilibrium diagrams are useful in determining the stable phases at a particular temperature and time. Equilibrium phase calculation for material A through TC analysis gave an idea of the phases that are expected to be present. It is seen from Figure 10 that all the carbides are dissolved, and austenite is stable at these conditions. Some of the phases are present only during the precipitation process as metastable carbides. The composition of the austenite phase is given in Table 5. Thus, the composition is the same as that in the hot-rolled sample, and this composition is further used in the precipitation calculations. In this simulation, even the vanadium carbides are dissolved which is contradicting the experimental results. Another simulation was run by including the elements in trace amounts, described in the next paragraph.

Table 5 Composition after austenization at 950°C for material A

Element	Fe	C	V	Mo
Mass %	98.46%	0.339%	0.14%	1.06%

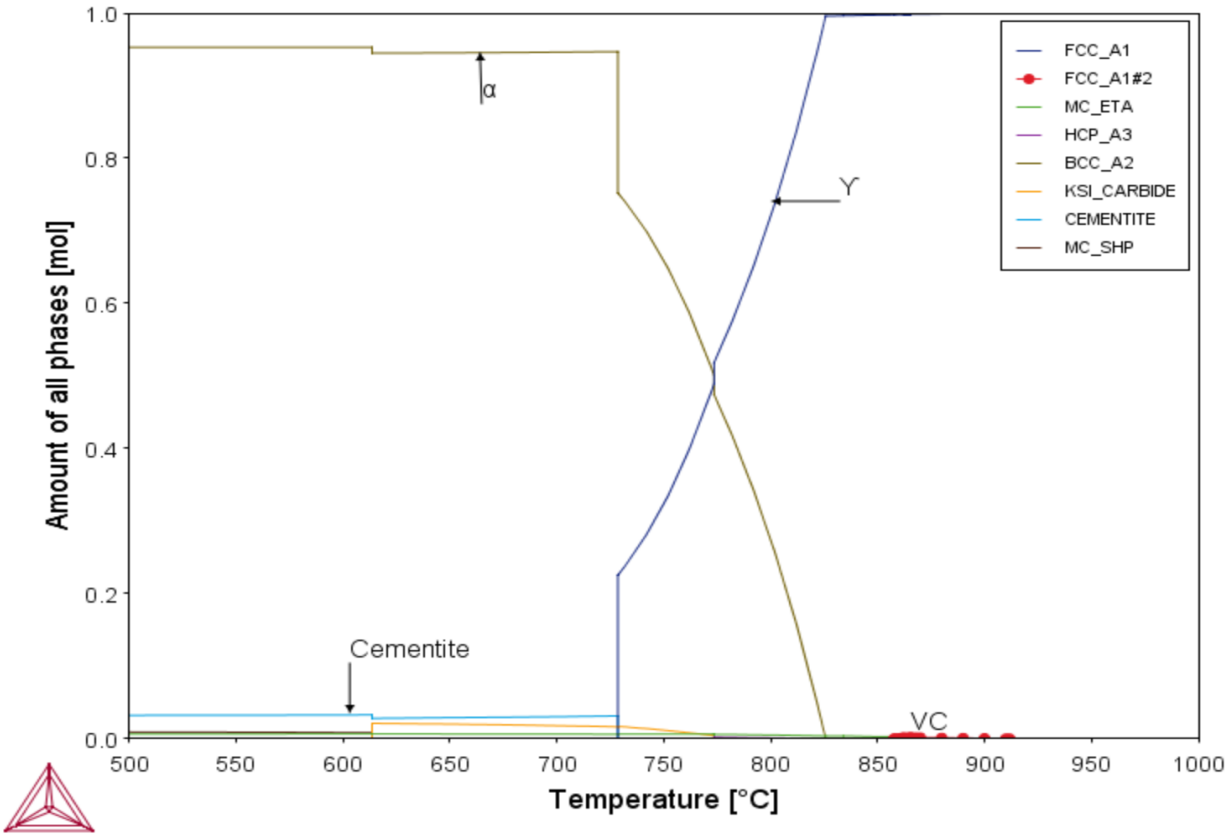

Figure 10 TC one axis equilibrium diagram in the system Fe-C-Mo-V for material A showing phases present at this temperature range, α: Ferrite, Y: Austenite, VC: vanadium-rich carbide.

However, when the one axis equilibrium calculation was run by including elements that are present in trace amounts, particularly nitrogen, it was seen that the vanadium-rich carbides already precipitated at the higher temperatures and were stable in the given temperature range, Figure 11. There was negligible change in the austenite composition and the composition mentioned in Table 5 was used. Therefore, it was assumed that no new vanadium-rich carbides nucleated during tempering. This is substantiated from the experimental results which depict that coarser vanadium-rich carbides are present in the as-quenched state and in the different tempering states, included in the next section. The precipitation calculation was therefore, run for the molybdenum-rich carbides and cementite to investigate the effect of tempering on the mean size, number density, and volume fraction of the precipitates. As stated earlier, the interfacial energy is referred from the references given in Table 6.

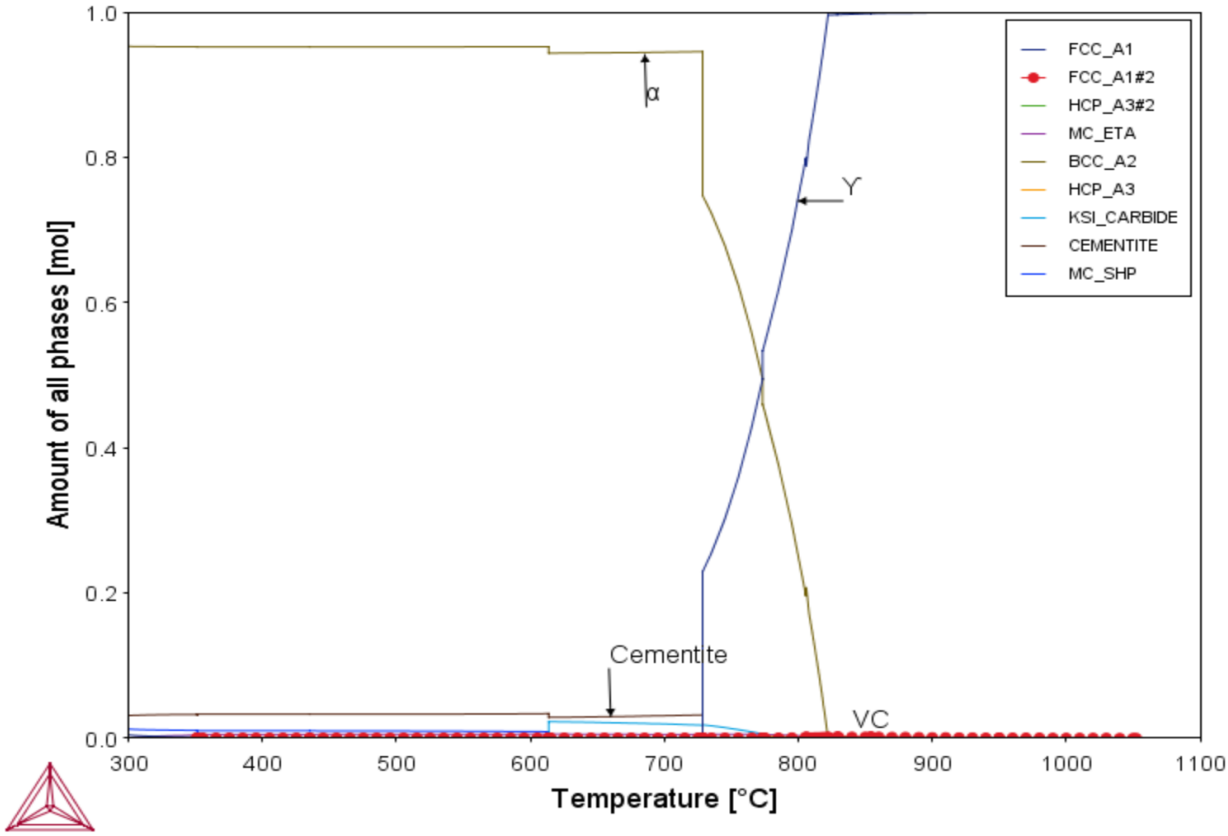

Figure 11 TC one axis equilibrium diagram including nitrogen in the system Fe-C-Mo-V for material A showing phases present at this temperature range, α: Ferrite, Y: Austenite, VC: vanadium-rich carbide.

Table 6 References for the interfacial energy

Reference	Value in Jm^{-2}	Matrix phase	Type of experiment
Stability of (Ti, M)C (M = Nb, V, Mo, and W) carbide in steels using first-principles calculations [50]	Fe-VC: 0.199 Fe-MoC0.5: 0.256	Ferrite	First-principle calculation of formation energies for alloying system (Ti,M)C, M = (Nb, V, Mo, W) in iron.
Modeling and characterization of V_4C_3 precipitation and cementite dissolution during tempering of Fe-C-V martensitic steel [51]	V_4C_3: 0.2	Ferrite	Simulation of precipitation during the tempering of martensitic steel in Fe-C-V ternary system.
Ab initio calculation of interfacial energies between transition metal carbides and fcc iron [52]	Bcc Fe/VC: 0.167	Ferrite	Ab initio study on coherent and semi-coherent interfacial energies for fcc Fe/MCs (NaCl structure, M = Ti, Zr, Hf, V, Nb, Ta) systems.
Modeling Precipitation of Carbides in Martensitic Steels [22]	Mo_2C: 0.2	Ferrite	Modeling of carbide precipitation in steels of a quaternary system which includes two substitutional elements (Si, Mn, Mo, V, N, Al)
Precipitation of molybdenum carbides in steel: Multi-component	Mo_2C/ α: 0.2481	Ferrite	Development of a methodology to deal with the growth of molybdenum carbide

diffusion and multi-component capillary effects [53]			in a ternary alloy (Fe–2Mo– 0·1C)
Ab initio study of energetics and structures of heterophase interfaces: From coherent to semicoherent interfaces [54]	Fe-on-C: 0.22, 0.35, 0.19, 0.26, 0.34, 0.39, 0.48	Ferrite	Calculation of the interfacial energies for the semi coherent interfaces with misfit dislocations.

The dislocation density is varied between $10^{13}m^{-2}$ to $10^{15}m^{-2}$. The interfacial energy for cementite and molybdenum carbide (with M_2C structure) is taken from the above references, from Property Model Calculator (Prisma calc in the diagram) and also varied to reproduce similar mean size as acquired from the experimental data. The mean diameter, number density, and volume fraction for material A tempered at 600ºC for 24 hours is mainly focused in these simulations and is given by Figure 12 to Figure 14. 'Prisma value' refers to those data where interfacial energy is calculated from the Property Model Calculator. It should be noted that the Prisma-calculated interfacial energy yields nearly no particles, as can be seen in Figure 13 and Figure 14 for number density and volume fraction, respectively, and is not a good value.

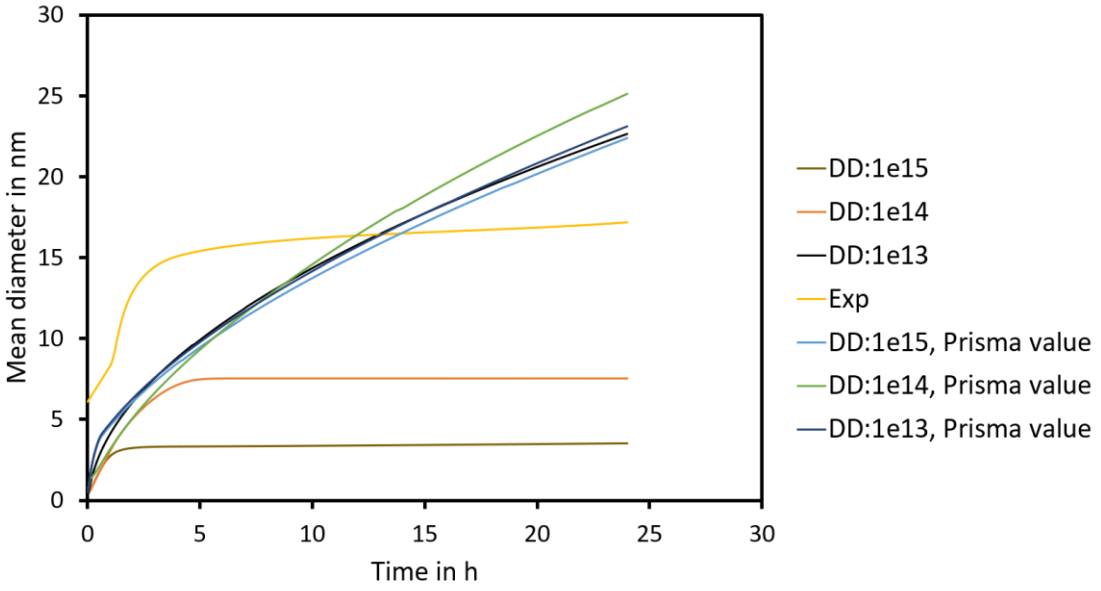

Figure 12 Prisma simulation for M_2C at 600ºC varying the dislocation density when interfacial energy is $0.3m^{-2}$ for cementite & $0.27m^{-2}$ for M_2C.

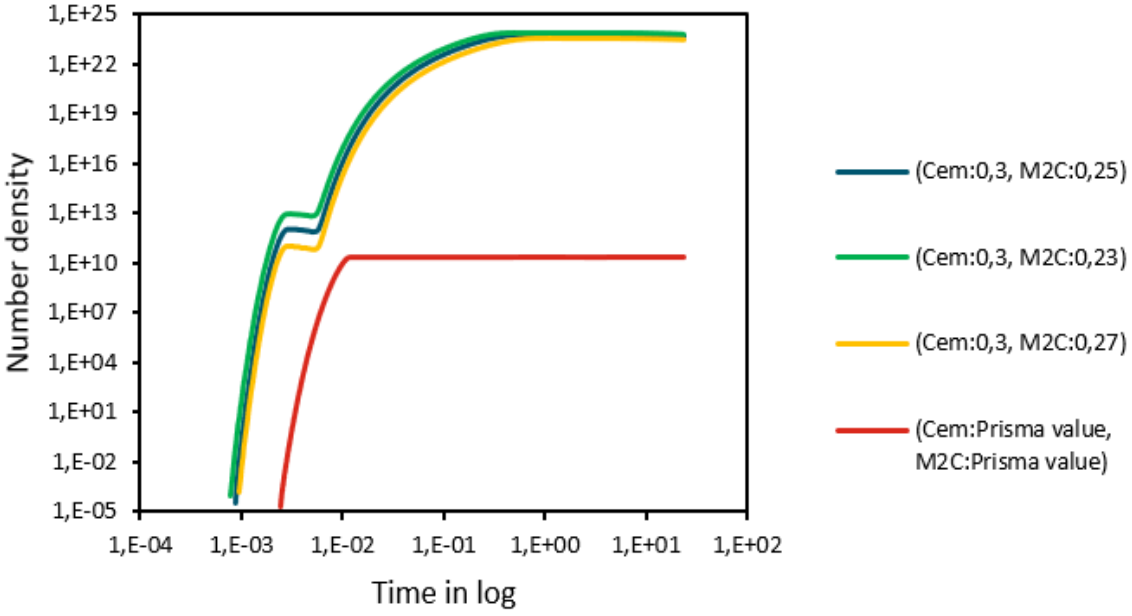

Figure 13 Prisma simulation for M_2C at 600ºC when interfacial energy is varied keeping dislocation density at $10^{15}m^{-2}$.

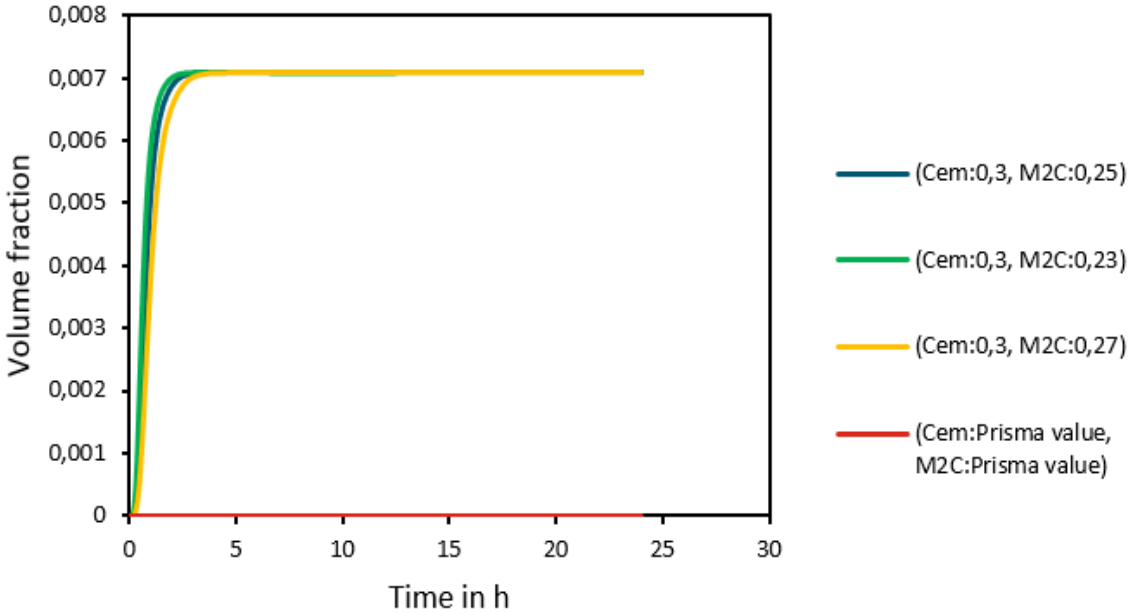

Figure 14 Prisma simulation for M_2C at 600ºC when interfacial energy is varied, keeping dislocation density at $10^{15}m^{-2}$.

4.2 HEAT TREATMENT

The heat treatment regime, as described in the experimental part, is shown in Figure 15 and Figure 16. These figures represent the cumulative heat treatment from austenizing until tempering at both the tempering temperatures.

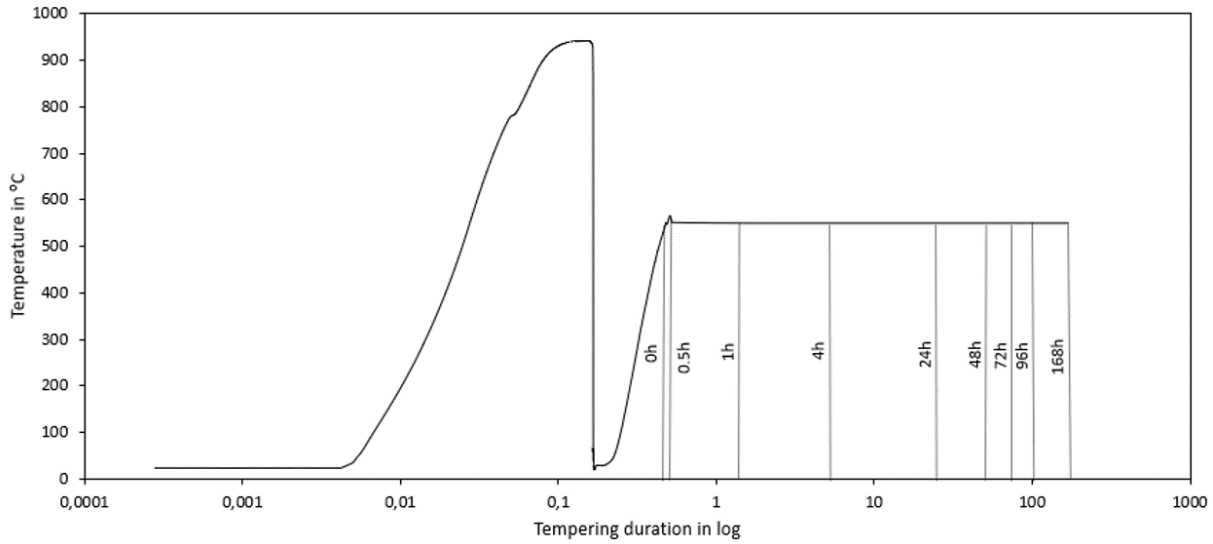

Figure 15 Heat treatment curve showing austenization and tempering at 550ºC.

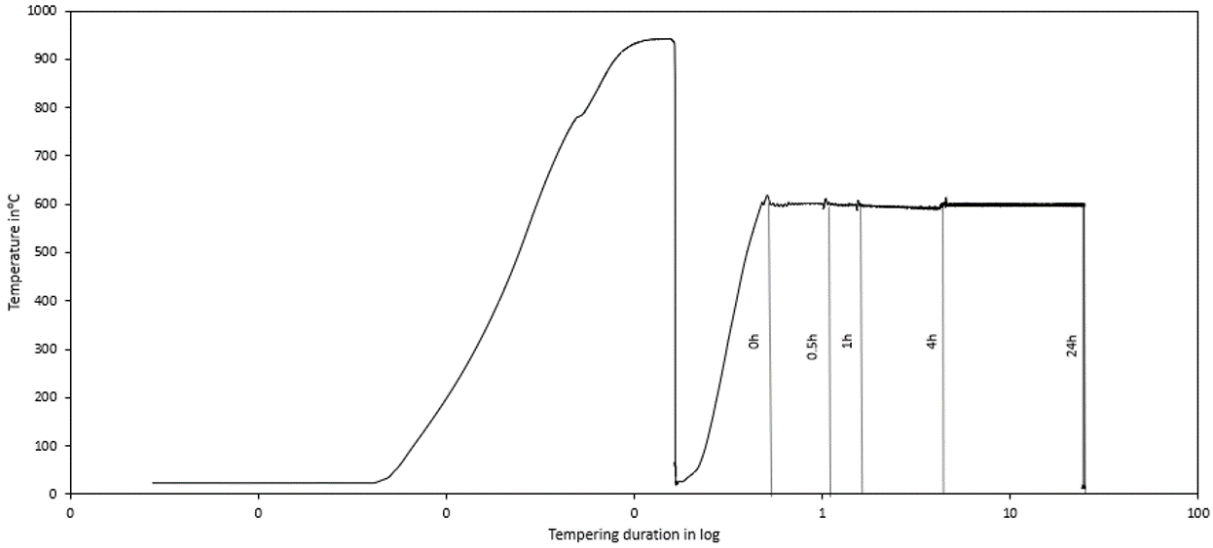

Figure 16 Heat treatment curve showing austenization and tempering at 600ºC.

4.3 LOM

The microstructure undergoes considerable changes during different tempering times and temperatures for both the materials. The microstructures obtained after austenization and tempering were captured under LOM. Figure 17 to Figure 21 show these images. Micrographs were taken of as-quenched state, and after 0h, 0.5h, 1h, 4h, and 24h of tempering for both the materials, A and B. Additional tempering was done for material A at 550ºC, to reach the hardness peak. Samples were tempered for 48h, 72h, 96h, and 168h; corresponding micrographs are given in Figure 18. It is in most of the areas that these variations, in contrast, are surrounded by lath boundaries, cementite, and secondary precipitates. The vanadium and molybdenum carbides are not visible in LOM since they are in the nanometer size range. The micrographs show an apparent tempering effect on the materials. They give a general idea of the steel structure. However, the overall microstructure images from LOM could not provide any factual

inferences regarding the precipitation of the nano-sized particles, and hence a more detailed STEM and EDS results were sought.

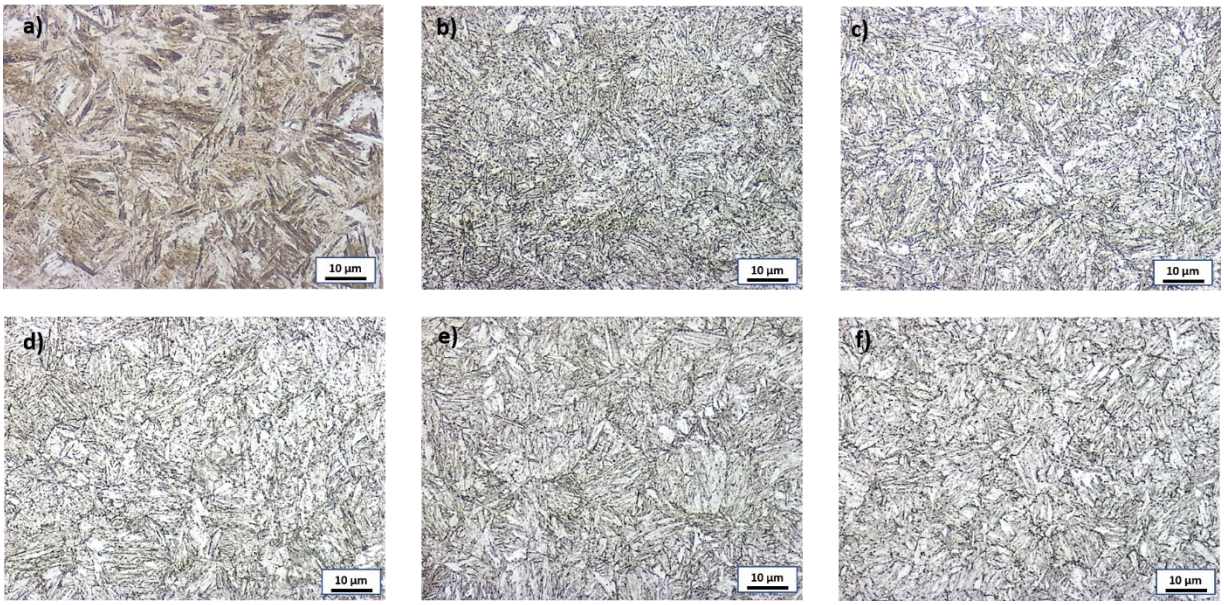

Figure 17 LOM microstructure for material A at a) AsQ b) 0h c) 0.5h d) 1h e) 4h f) 24h of tempering at 550ºC.

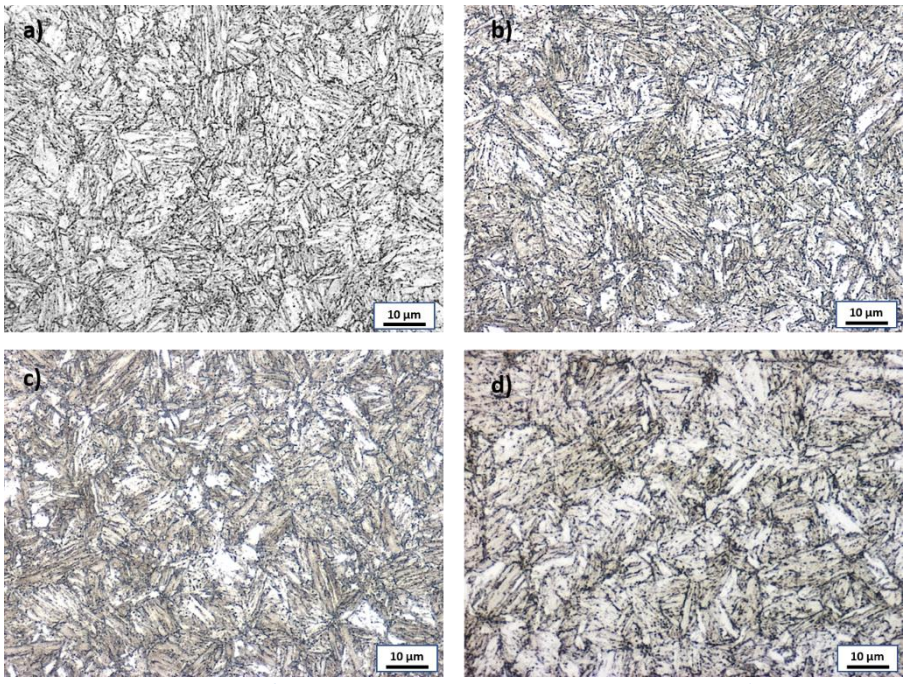

Figure 18 LOM microstructure for material A at a) 48h b) 72h c) 96h d) 168h of tempering at 550ºC.

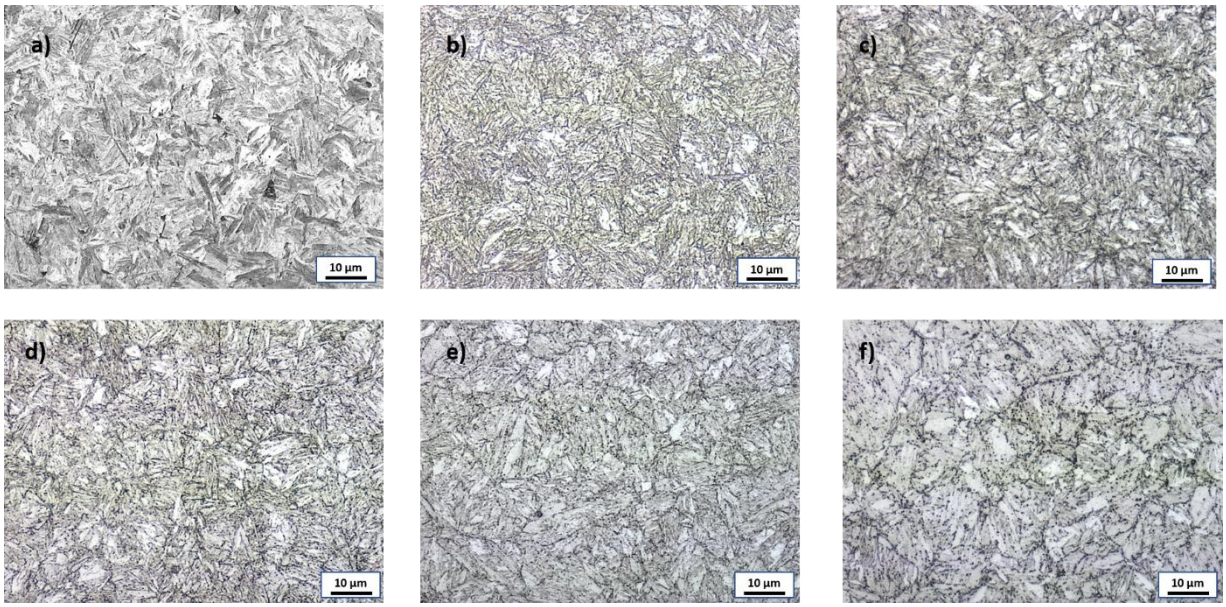

Figure 19 LOM microstructure for material A at a) AsQ b) 0h c) 0.5h d) 1h e) 4h f) 24h of tempering at 600ºC.

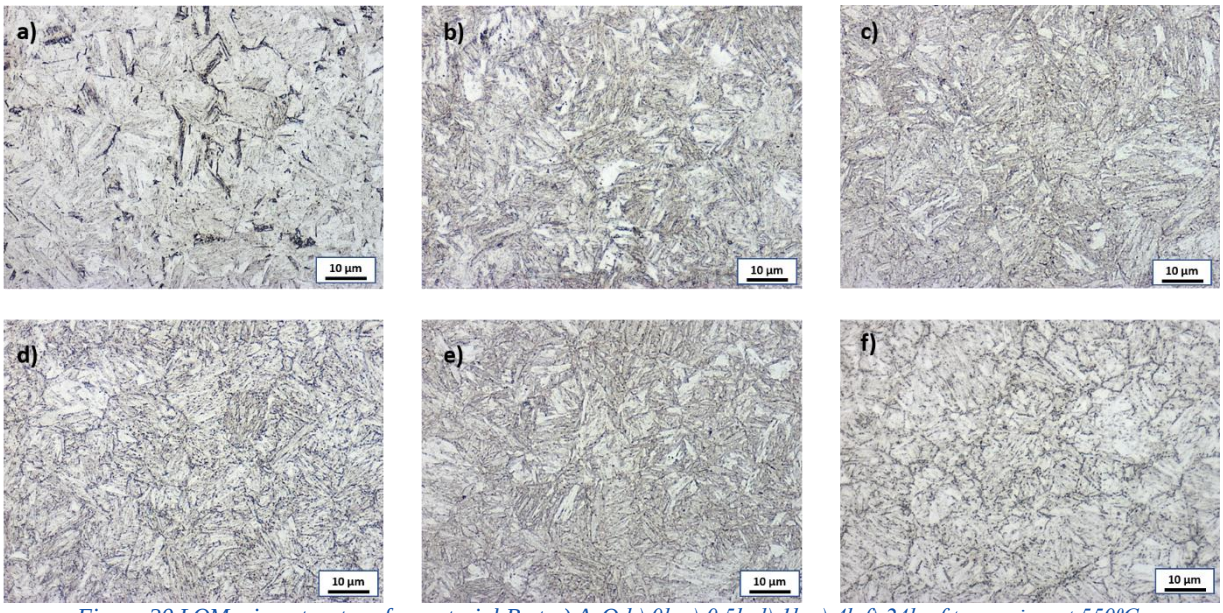

Figure 20 LOM microstructure for material B at a) AsQ b) 0h c) 0.5h d) 1h e) 4h f) 24h of tempering at 550ºC.

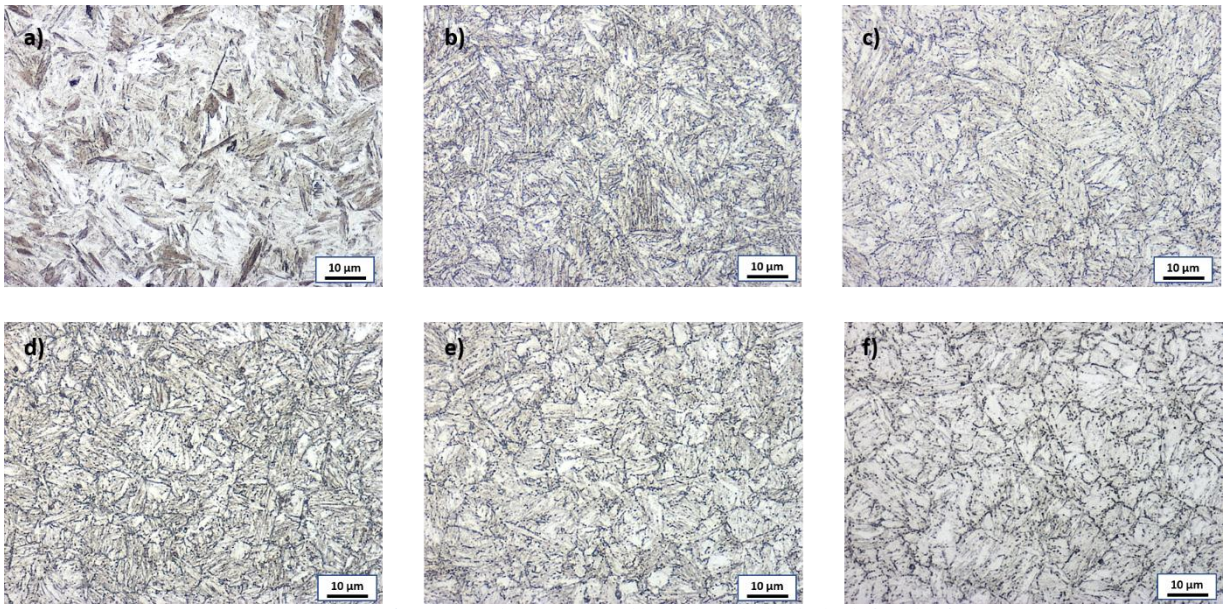

Figure 21 LOM microstructure for material B at a) AsQ b) 0h c) 0.5h d) 1h e) 4h f) 24h of tempering at 600ºC.

4.4 VICKERS HARDNESS

From the hardness results, it is clear that the hardness of material A is higher than that of material B at both the tempering temperatures, 550ºC and 600ºC. This could be due to the higher molybdenum content in material A. Hardness curves at both the temperatures show a sharp decline in the hardness from as-quenched state to 0h for materials A and B, Figure 22 and Figure 23. For material A, at 550ºC, the hardness follows alternate trends in which the hardness decreases and increases until 24h, Figure 22. The hardness increases after 24h and stabilizes up to 96h, after which the hardness slightly decreases up to 168h. Material B at 550ºC follows a similar pattern up to 24h, Figure 23. The overall thermodynamics and kinetics processes at 550ºC are slower compared to 600ºC. Hence, longer tempering times for 550ºC are required to reach the hardness peaks by both the materials, Figure 24. The hardness at 600ºC gradually increases from 0h to 0.5h until 4h of tempering and decreases at 24h for both the materials, Figure 25. For material A at 600ºC, the hardness peak is reached after 4h in contrast to material B at 600ºC, Figure 25 where hardness has already reached its peak after 1h.

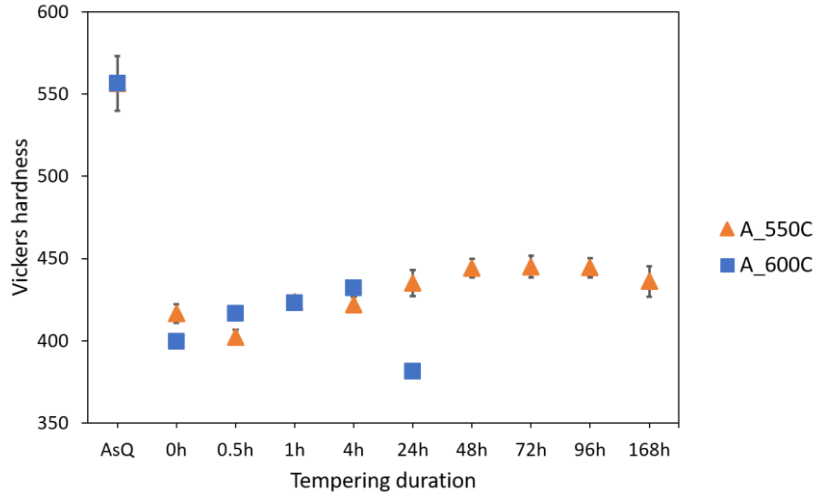

Figure 22 Hardness measurements for material A at temperatures 550ºC and 600ºC.

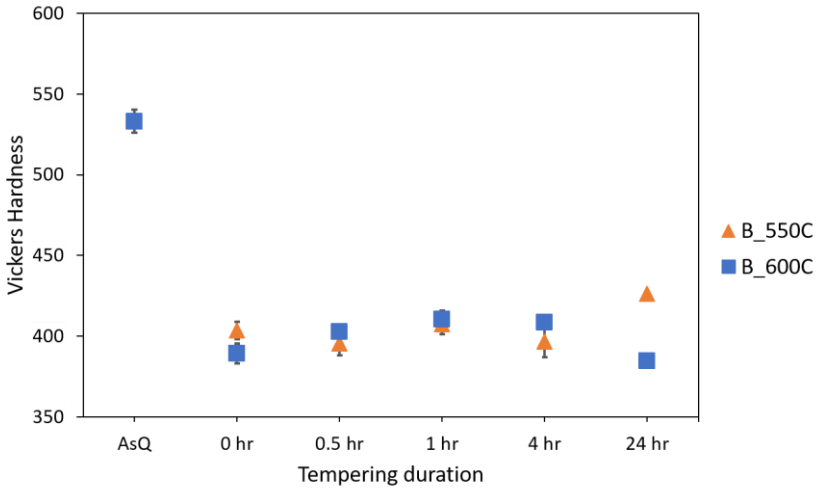

Figure 23 Hardness measurements for material B at temperatures 550ºC and 600ºC.

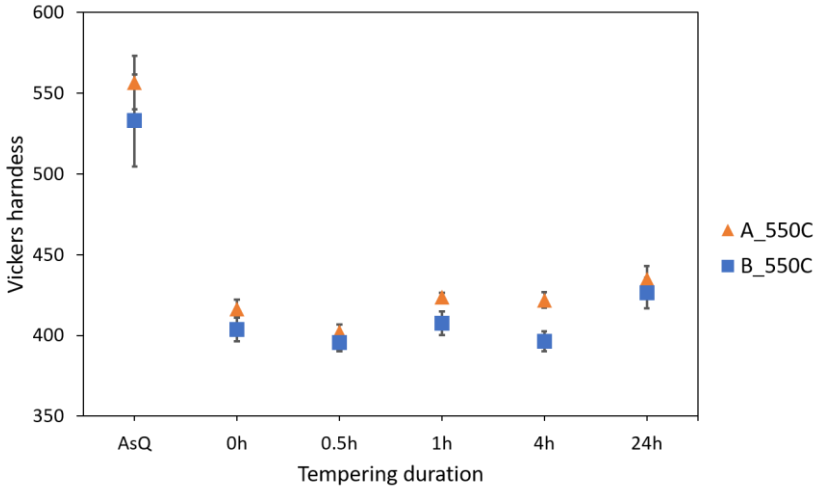

Figure 24 Hardness comparison for materials A and B at 550ºC.

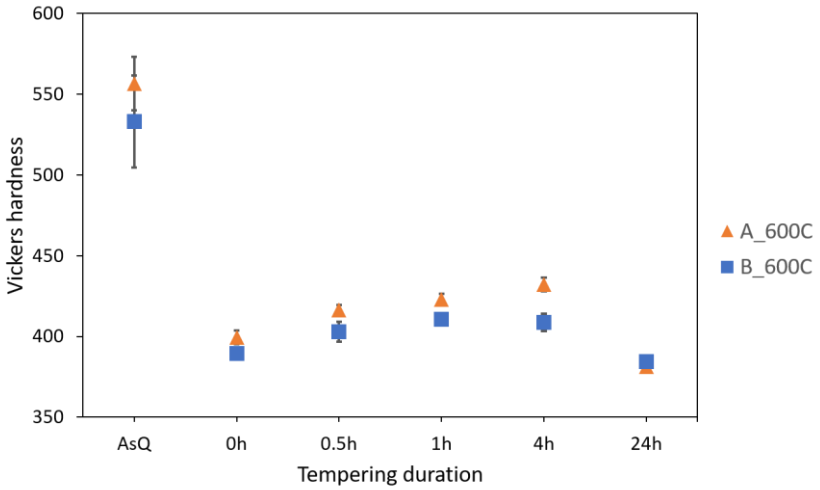

Figure 25 Hardness comparison for materials A and B at 600ºC.

4.5 STEM

The BF images Figure 26 and Figure 27 focus on the overview of the microstructure at different tempering times, and the DF images Figure 28 and Figure 29, represent the precipitates for material A. Figure 26 and Figure 27 show the BF images of carbon replicas. From the as-quenched state up to 168h for 550ºC and up to 24h for 600ºC, for material A, precipitation, growth, and coarsening of secondary carbides, as well as cementite, is taking place simultaneously. The size of the carbides increases across the tempering times. From 0h of tempering until 24h, there is a drastic increase in the presence of carbides. This is more pronounced for material A at 600ºC than at 550ºC. In the as-quenched state, imprints of martensitic lath boundaries and/or prior austenite grain boundaries are also seen (shown as blue arrows in Figure 26) in the BF images that eventually disappear at higher times of tempering. This could be because of the dissolution of the martensitic structure in the matrix that takes place in some areas due to the formation of transition carbides, cementite, and other secondary precipitates. It is important to note that the martensite matrix retains some of the morphological features even after tempering [17]. The secondary carbides and cementite is more clearly seen in the dark field images Figure 28 and Figure 29. Cementite is the large particle, as shown by the orange arrows. Numerous small particles nucleate and grow continuously during the tempering process. These particles are generally irregular but also appear to be spherical, rod-like, and elongated in morphology. The carbides nucleate and grow on dislocations [6][22], appearing prominently at 4h for both the temperatures in Figure 28. There is a variation in contrast at different parts of the images in dark field mode. This is due to the difference in the carbon film thickness across the copper grid that provides differing contrast in appearance.

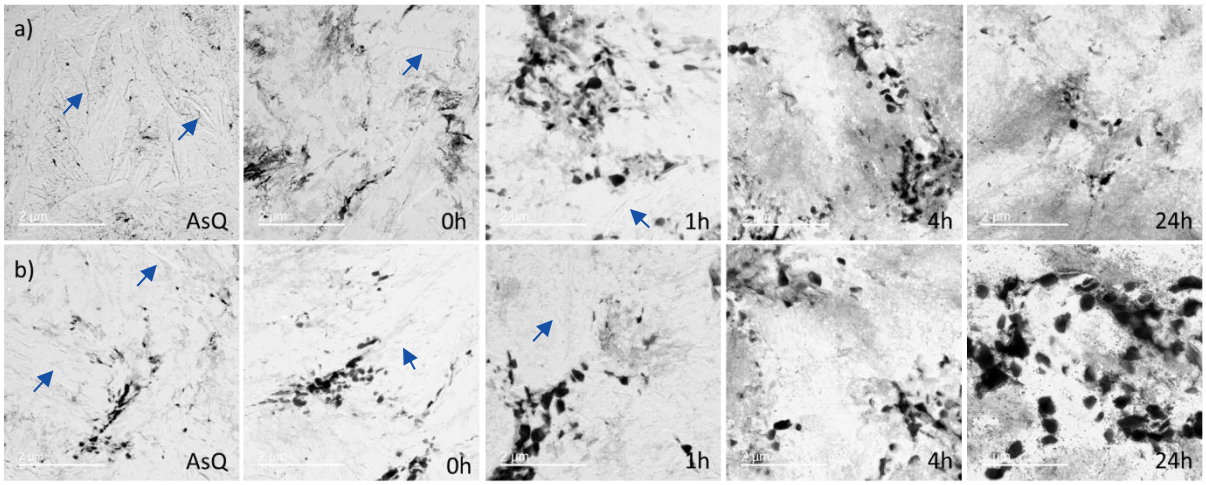

Figure 26 BF images for a) 550ºC b) 600ºC for material A at different tempering times. The arrows show martensitic lath boundaries/ prior austenite grain boundaries.

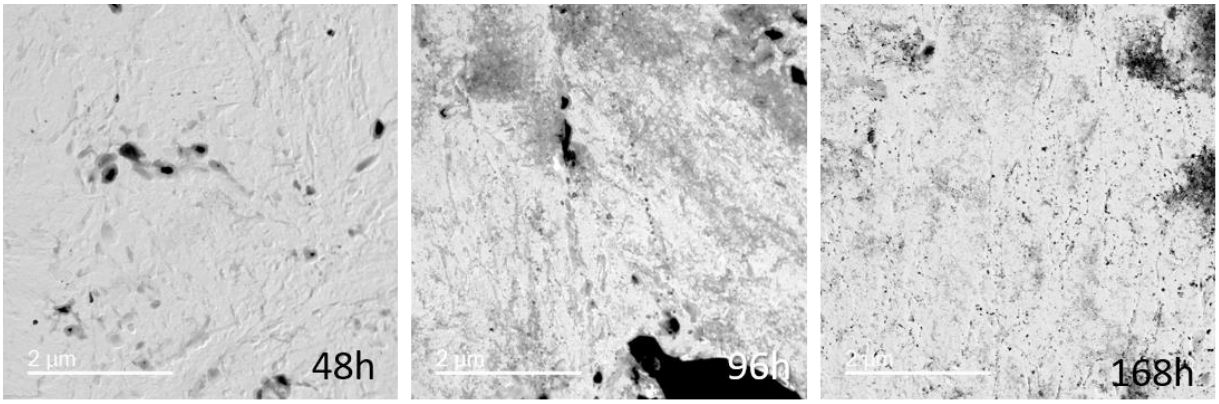

Figure 27 BF images for material A at 550ºC for increased tempering duration.

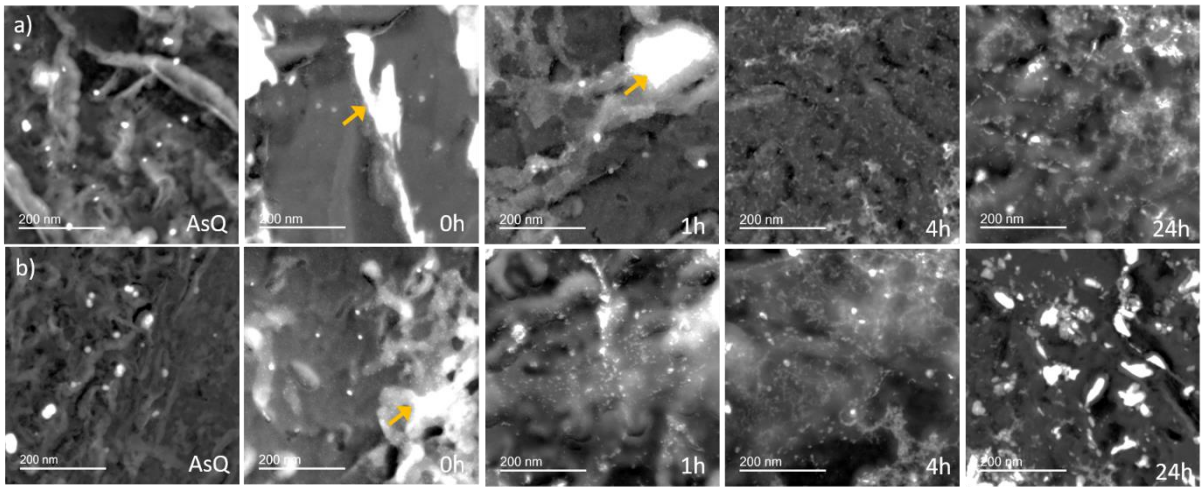

Figure 28 DF images for a) 550ºC b) 600ºC for material A at different tempering times. The arrows show cementite.

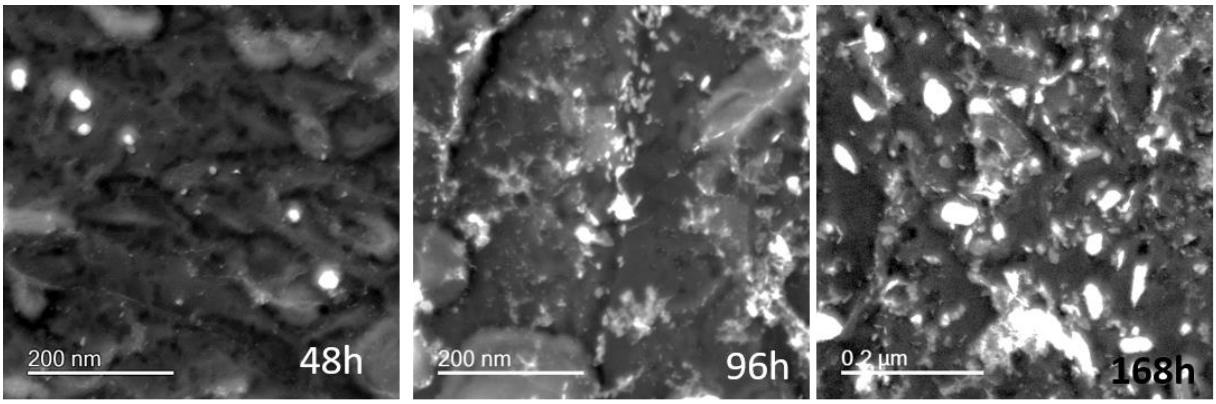

Figure 29 DF images for material A at 550ºC for increased tempering duration.

4.6 EDS

X-ray spectra were acquired for enumerable particles pointwise. Based on the spectral analysis, the particles were identified as vanadium/molybdenum carbides. Figure 30 represents how elemental mapping of a point chosen is done with STEM-EDS. This is the state of the microstructure of material A tempered at 600ºC for 1h. Among our elements, vanadium, molybdenum, and iron, the spectra with the highest intensity is considered to be the element rich in that particle. Hence, as depicted in this Figure 30 there are vanadium-rich (pink arrow) and molybdenum-rich (blue arrow) carbides in this state of tempering for material A. EDS data for all the other samples of material A at 550ºC and 600ºC at different tempering times were obtained to study the presence of vanadium-rich and/or molybdenum-rich particles in the matrix. This is presented in Figure 31 to Figure 33 for the as-quenched state, at 550ºC and 600ºC, respectively.

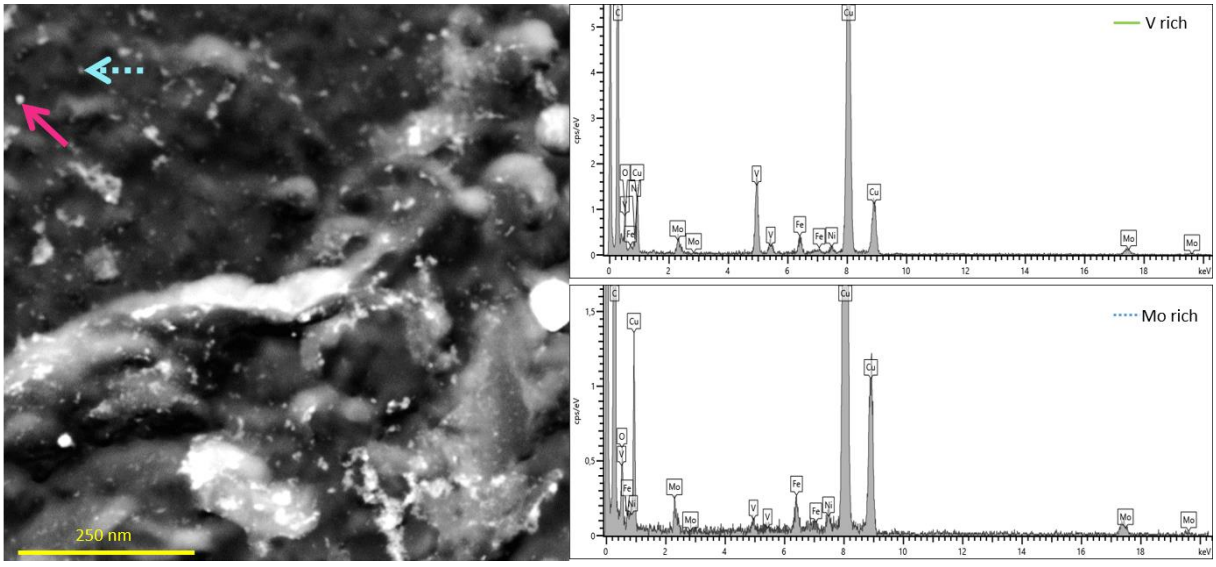

Figure 30 An example of EDS spectra analysis for material A, 600º at 1h of tempering.

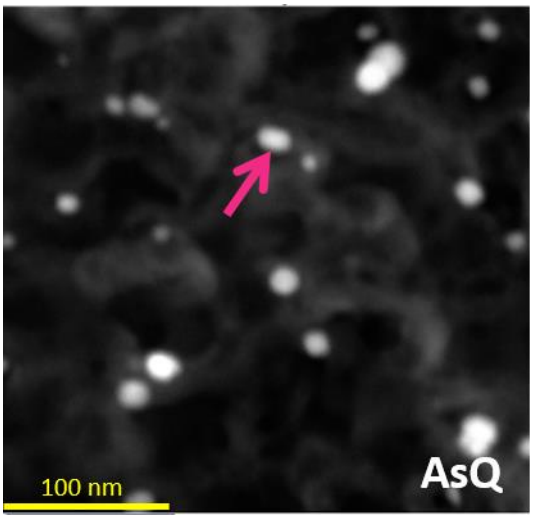

Figure 31 STEM-EDS image showing the vanadium-rich (pink arrow) carbide for material A in the as-quenched state.

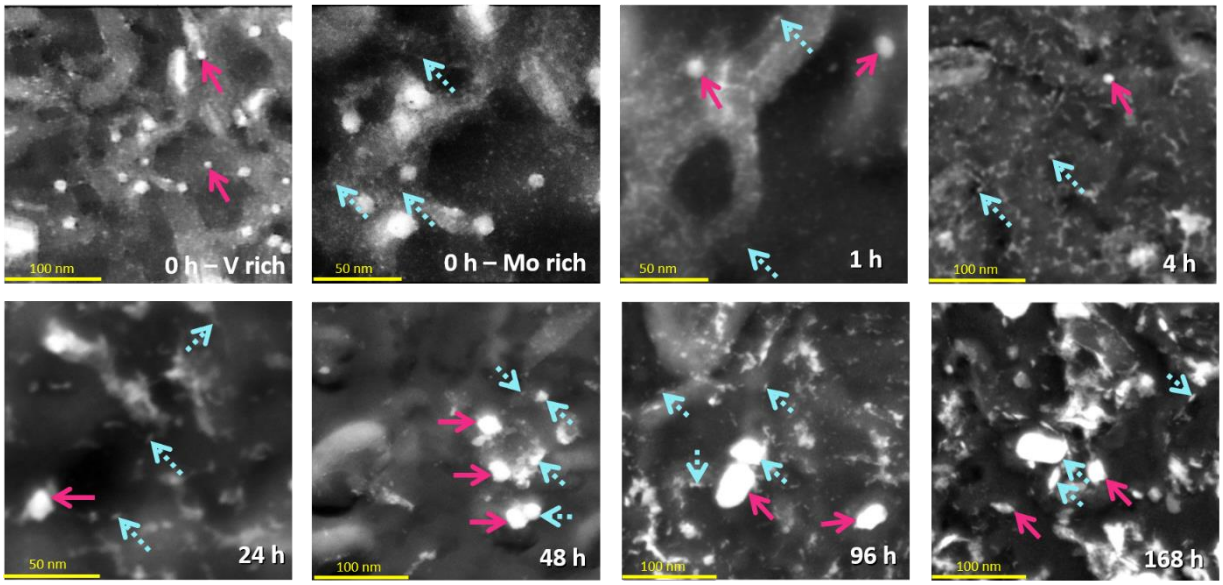

Figure 32 STEM-EDS images with arrows showing the vanadium-rich (pink arrows) and molybdenum-rich carbides (blue arrows) for material A at 550ºC for different tempering durations.

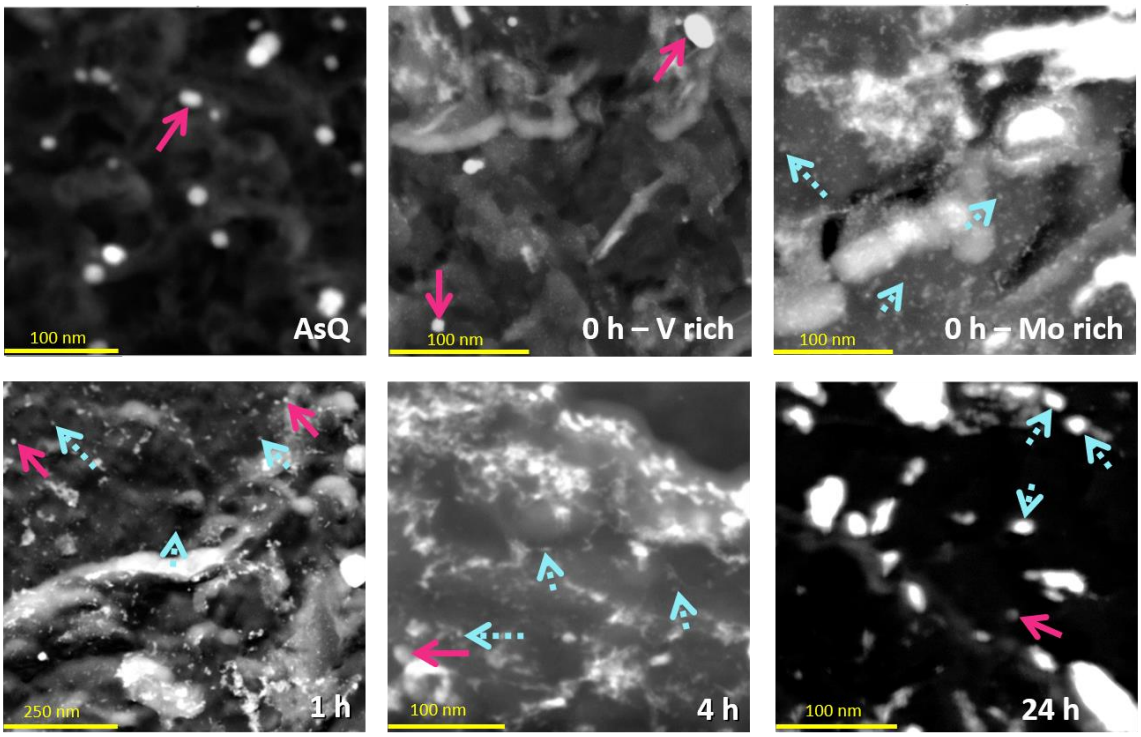

Figure 33 STEM-EDS images with arrows showing the vanadium-rich (pink arrows) and molybdenum-rich carbides (blue arrows) for material A at 600ºC for different tempering durations.

4.6.1 CHEMICAL COMPOSITION

The relative atomic percentage of the individual elements in vanadium-rich and molybdenum-rich carbides in the different tempering stages can be seen from the composition histograms in Figure 34 to Figure 37. The atomic percentage of vanadium, molybdenum, and iron in the corresponding vanadium-rich and molybdenum-rich carbides vary across the tempering durations. An irregular trend at 550ºC is witnessed for both the types of carbides. This could be due to the slow kinetics of the process as compared to that at 600ºC. Enrichment of the vanadium-rich carbides by molybdenum and iron; and molybdenum-rich carbides by vanadium and iron are taking place during tempering. There are also instances at which the iron percentage is significant than vanadium and/or molybdenum in the vanadium-rich and molybdenum-rich carbides, respectively.

The chemical composition histograms correspond to the top 20 particles based on their composition under the different carbide types. This was done to avoid the effect of beam drift that was persisting during the EDS analysis. The particles that indicated a higher composition from the intensity of the spectra were assumed to have no drift and vice versa. During the investigation, the central points in the particles were chosen approximately. It was noticed that the EDS spectra from the smaller particles had a mixed measurement from the particle and the background of the replica that could be the reason for the lower spectral intensities of the desired elements (Mo, V). Further, it is assumed that the composition of small and big particles is the same. However, following this, it was realized that the size of the carbides was overestimated. Hence, log-normal size distribution was used to represent the overall size distribution of these carbides. The data was fitted for attaining a probable size distribution. The mean (μ) and the standard deviation (σ) of the distribution were acquired. This is described in the next section.

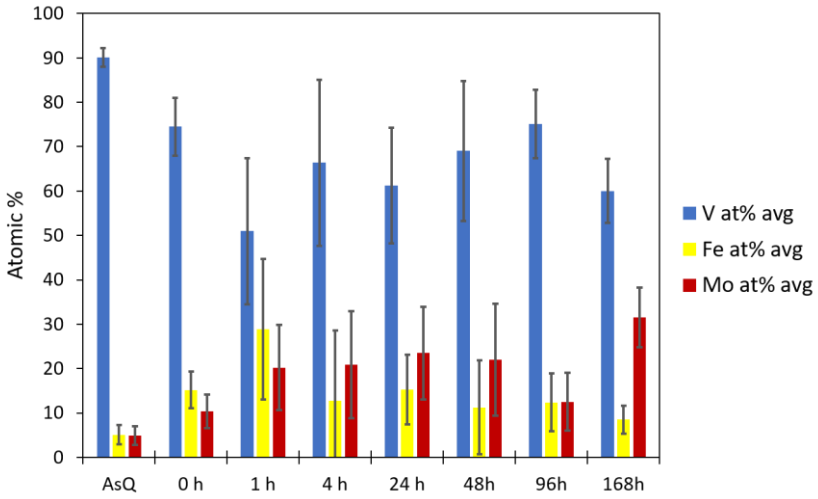

Figure 34 EDS chemical composition histogram of material A for vanadium-rich carbides at 550ºC.

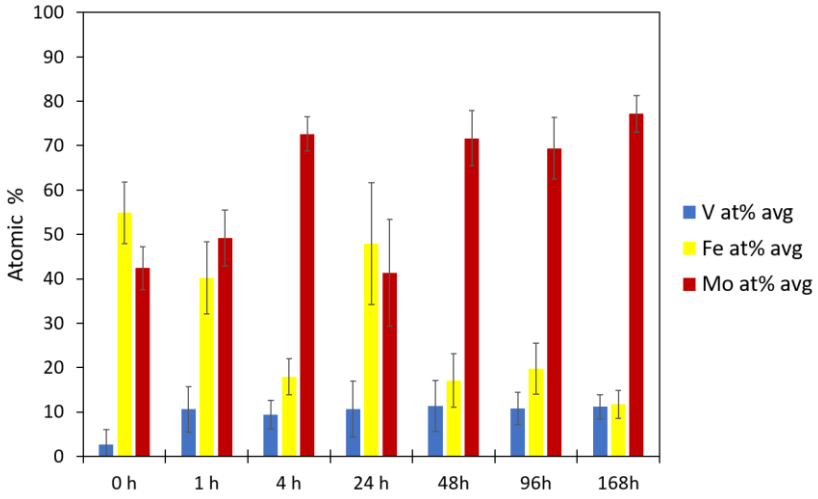

Figure 35 EDS chemical composition histogram of material A for molybdenum-rich carbides at 550ºC.

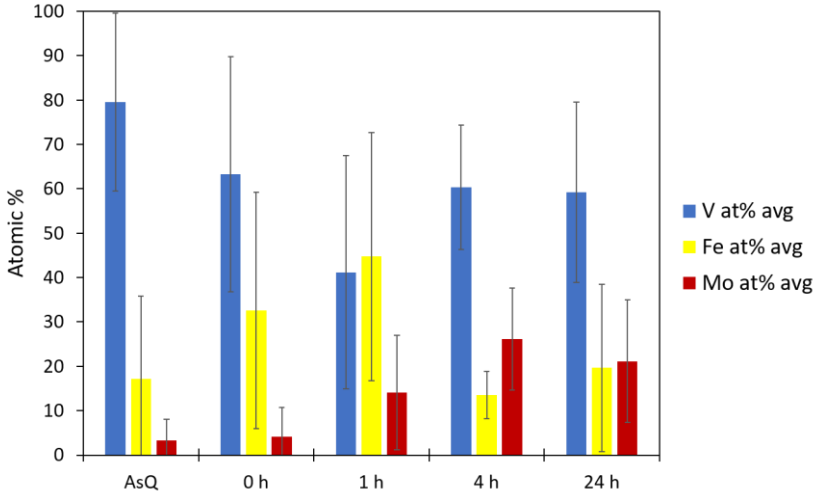

Figure 36 EDS chemical composition histogram of material A for vanadium-rich carbides at 600ºC.

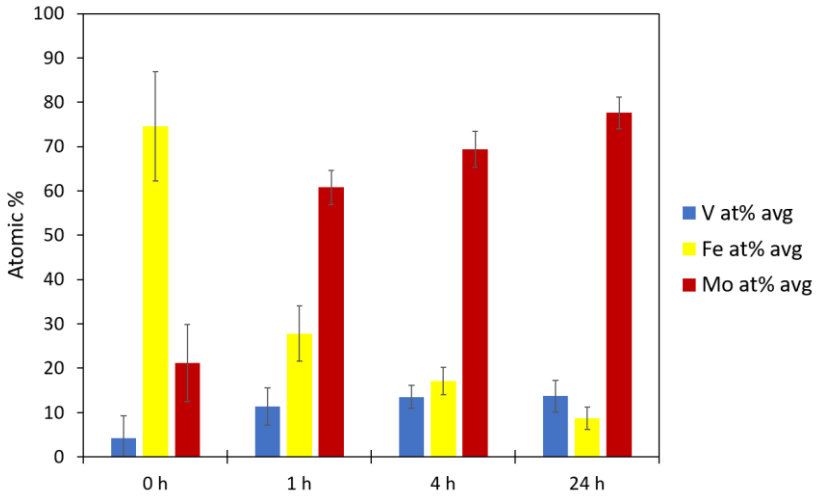

Figure 37 EDS chemical composition histogram of material A for molybdenum-rich carbides at 600ºC.

4.6.2 PARTICLE SIZE DISTRIBUTION

Based on the STEM-EDS results, the particles were identified. The size of these particles was measured manually using Aztec. The equivalent circular diameter of the particles was taken into consideration to set a common comparison standard for the different morphologies of all the particles. Equivalent circular diameter is the average of the longest distance and the perpendicular shortest distance of the particle in nanometers. It is important to note that there were separate as-quenched state samples at 550ºC and 600ºC for material A. This was done to maintain homogeneity in further experimental verification. Since the as-quenched state was the same irrespective that different samples were taken to assure the homogeneity, the log-normal size distribution curve was taken for the average of both of these samples. The description of the number of particles analyzed, the mean diameter in nanometers, and the standard deviation of the particles in the as-quenched state is given in

Table 7. The mean diameter and the standard deviation correspond to the mean (μ) and the standard deviation (σ) of the log-normal particle size distributions, shown in Figure 38. The mean diameter is the exponent of μ and standard deviation is the exponent of σ.

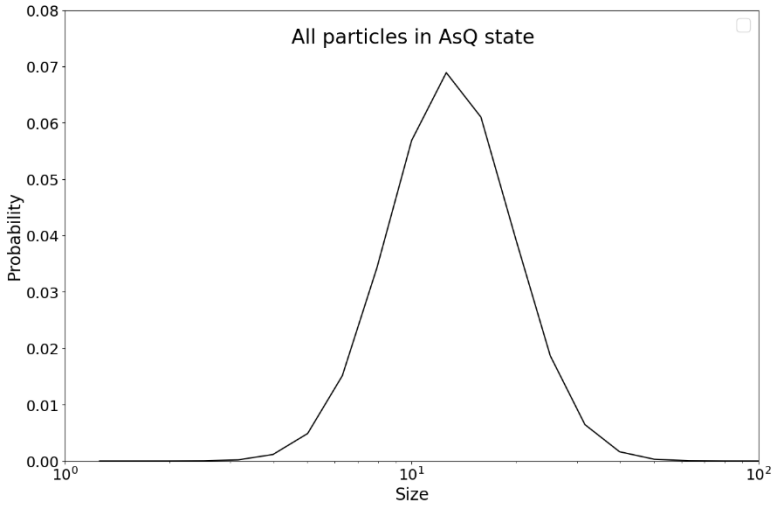

Figure 38 Log-Normal particle size distribution of all the particles in the as-quenched state for material A.

Table 7 Mean diameter and the standard deviation of the particles in the as-quenched states at both temperatures for material A

Number of particles	Mean (μ) from the distribution	Mean diameter exp(μ) in nm	Standard deviation (σ) from the distribution	Standard deviation exp(σ)
156	2.7	15.3	0.4	1.5

Fitting is a significant step in analyzing the data. This is used to obtain a statistical distribution that best fits the data. It means that the fit is able to express our data implicitly. The possibilities reflected from the fit must be consistent and predictable based on our data. There are various statistical techniques that help to determine the best fit. Distribution parameters such as location, shape, scale, and threshold can be used to identify the best fit. A more convenient way is to visually recognize the best fit by plotting a histogram that is overlapped by the distribution [55] [56]. For my data on the size of the particles, I have made use of the visual technique to identify the best fit. An example of a good fit is given in Figure 39. The data is that of vanadium-rich particles in material A, tempered at 550ºC for 168h.

The size distribution depicted by the histogram is concentrated on a rather smaller region on the x-axis, which is the logarithm of the size of the particles. Fitting was done to indicate the data conveniently. From the bad fit, it is difficult to predict the probability of the particles that would fall in size range when the data is missing. This gap is best filled by a good fit that provides a likelihood of those particles that are not included in the data. It is necessary to consider that the size of the particles was measured manually using Aztec after identifying the particle type by the EDS measurements. Not all the particles present in the matrix could be verified, and it was assumed that the smaller and the bigger particles had the same chemical composition. Beam drift, screening of the spectra by the copper grid, and the thickness variation of the carbon replica posed limitations in acquiring a large amount of data. Also, the carbon deposition in the investigating area of the copper grid limited the number of instances of the spectrum analysis.

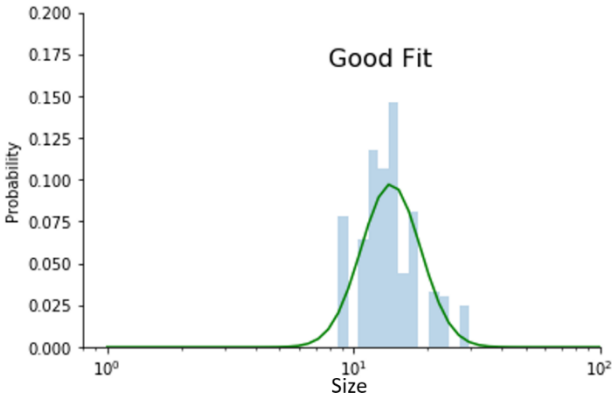

Figure 39 An example of a good fit.

The number of particles estimated for each carbide type at different tempering duration is given in Table 8 and Table 9. The mean diameter and the standard deviation correspond to the mean (μ) and the standard deviation (σ) of the log-normal particle size distributions. The mean diameter is the exponent of μ and the standard deviation is the exponent of σ of the distribution. From the tabulated data, it is seen that the size of the molybdenum-rich carbides increases with increasing tempering times at both the tempering temperatures, whereas for the vanadium-rich carbides, the size is approximately similar as in the as-quenched state. However, the number of particles analyzed for each sample type puts a check on the inferences derived from this data. The lesser the number of particles analyzed, the more the uncertainty in the measurement.

Table 8 Mean diameter and standard deviation obtained from the log-normal size distributions for the number of particles of each carbide type at 550°C for material A

Tempering duration	Mean (μ) from the distribution		Mean diameter exp(μ) in nm		Standard deviation (σ) from the distribution		Standard deviation exp(σ)		Number of particles analyzed	
	V rich	Mo rich	V rich	Mo rich	V rich	Mo rich	V rich	Mo rich	V rich	Mo rich
0h	2.3	1.5	10.4	4,5	0.3	0.7	1.4	1.9	32	46
1h	2.4	1.7	11.2	5.7	0.4	0.5	1.5	1.7	16	71
4h	2.7	1.9	15.3	6.7	0.3	0.5	1.4	1.7	11	107
24h	2.8	2.0	15.8	7.4	0.4	0.6	1.5	1.8	27	48
48h	2.8	1.9	15.8	6,7	1.0	0.8	2.7	2.2	20	79
96h	2.6	2.1	12.9	8.3	0.6	0.6	1.8	1.8	15	120
168h	2.7	2.1	15.3	8.3	0.3	0.6	1.4	1.8	15	87

Table 9 Mean diameter and standard deviation obtained from the log-normal size distributions for the number of particles of each carbide type at 600°C for material A

Tempering duration	Mean (μ) from the distribution		Mean diameter exp(μ) in nm		Standard deviation (σ) from the distribution		Standard deviation exp(σ)		Number of particles analyzed	
	V rich	Mo rich	V rich	Mo rich	V rich	Mo rich	V rich	Mo rich	V rich	Mo rich
0h	2.7	1.7	14.7	5.8	0.6	0.3	1.7	1.4	51	29
1h	2.4	1.9	10.6	6.8	0.6	0.6	1.9	1.9	11	56
4h	2.8	2.5	17.2	12.2	0.4	0.6	1.5	1.9	4	118
24h	2.7	2.7	14.7	14.2	0.5	0.6	1.6	1.9	9	110

Interestingly, from STEM, EDS and PSD results, it is seen that the vanadium-rich carbides (shown as red dots) are already present in the as-quenched state. They might have stayed from the hot rolling and stabilized by other elements like nitrogen present in trace amounts in the matrix [57][58][59][60]. The amount of the vanadium-rich carbides is very low in the matrix and are present in the temperature range between 350°C to 1050°C approximately, from the TC results, Figure 11. Austenizing the steels at 950°C did not dissolve all the carbides, and prolonged austenization would have resulted in increased grain size [8], which was undesirable. However, these coarse vanadium carbides did not affect the hardness considerably, and hence the experiments were continued.

5 DISCUSSION

5.1 TC–PRISMA

In the simulation, it was assumed that dislocations are the nucleation sites for the carbides. The dislocation density was varied to note the effect on the size of the molybdenum-rich carbides. Figure 12 shows that the mean diameter increases as the dislocation density decreases from $10^{15}m^{-2}$ to $10^{13}m^{-2}$. The decrease in the dislocation density reduces the number of potent nucleation sites. This leads to fewer particles precipitating at these sites. Fewer particles lead to larger particles if growth is completed. Varying the interfacial energy for both cementite and molybdenum carbide, it was realized that according to the Prisma calculated values, the growth of carbides surpasses the experimental data, which is not satisfactory. This tendency was also seen when the dislocation density was set to $10^{13}m^{-2}$. However, when the interfacial energies are kept similar for cementite (0.25 Jm^{-2}) and molybdenum carbide (0.25 Jm^{-2}) and the dislocation density is $10^{13}m^{-2}$, the size reached at 24 hours is close to the experimental data, Figure 40. When dislocation density was set at higher dislocation density values, the calculation was not converging for the interfacial energy of cementite (0.25 Jm^{-2}) and molybdenum carbide (0.25 Jm^{-2}) .

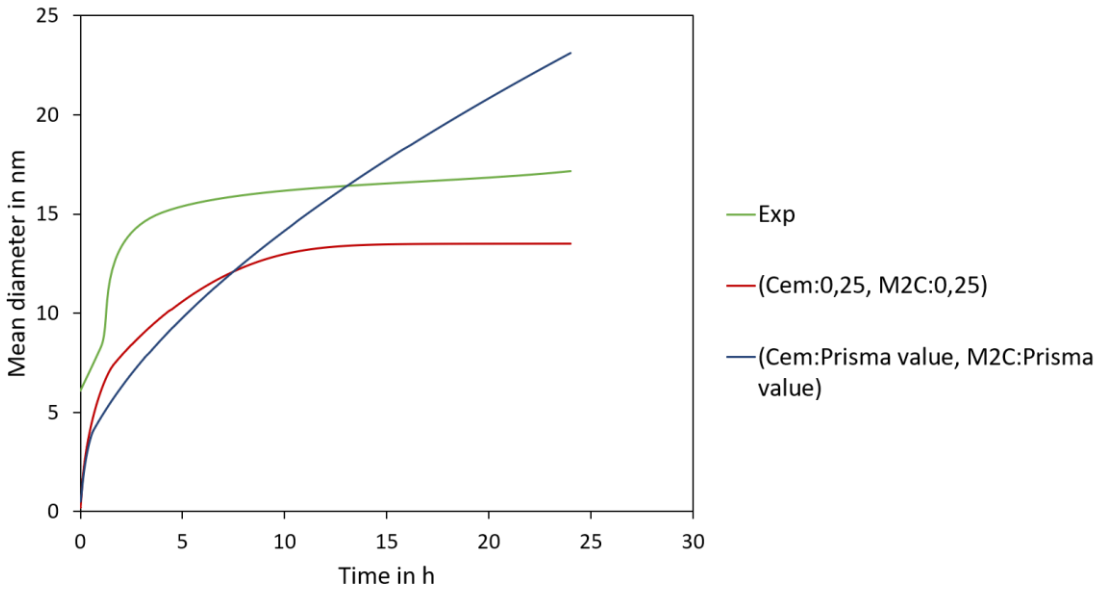

Figure 40 Prisma simulation for M_2C at 600°C, where the dislocation density is $10^{13}m^{-2}$.

As seen from Figure 13 and Figure 14, the number density and volume fraction of the particles is underestimated when the interfacial energy is calculated by the Property Model Calculator, where the values of the interfacial energy calculated for cementite is 0.16 Jm^{-2} and for the molybdenum carbides is 0.54 Jm^{-2} for material A at 600°C. In contrast to these values, the interfacial energy taken from the references and those that were modified later in the simulations were 0.3 Jm^{-2} for cementite and varied between 0.23 Jm^{-2}, 0.25 Jm^{-2} and 0.27 Jm^{-2} for molybdenum carbides. Lower interfacial energy leads to easy nucleation of the precipitates in the matrix as the Gibbs energy is less [26]. Thus, high interfacial energy of molybdenum carbides from the Property Model Calculator can be one of the reasons to give such low values for the number density and the volume fraction of the carbides.

The simulation results for $10^{15}m^{-2}$ for the mean diameter shows that the size at 24 hours is very small when compared with the experimental data. As no data could be acquired for the number density and volume fraction from the STEM-EDS investigations, a comparison between experimental data is not possible for these parameters. This is one of the practical limitations of the STEM-EDS characterization technique due to time constraints of the thesis. But the large difference between the experimental size and the simulated size makes it necessary to consider whether the dislocation density must be reduced or other factors in the simulation must be looked upon, such as the mobility enhancement factors. Further, the isothermal precipitation calculation in Prisma did not mimic the experimental heating rate, and the interfacial energies of the carbides are constant throughout the calculation.

In general, the precipitation results give an idea of how the carbides are evolving in terms of size, number density, and volume fraction for a better understanding of the precipitation process. However, it is also necessary to conduct more experimental verifications regarding these parameters by focusing on a particular area in the sample and characterizing all the particles using STEM-EDS for mean diameter, number density and volume fraction, similar to [22][61]. This will provide a basis to relate to the precipitation model. The application of thermodynamic extremum principle to model the precipitate structure via matrix diffusion as in [62], inverse modeling of the experimental data to obtain the interfacial energy as in [49][63], measurement of the dislocation density from microhardness as in [64] are some of the examples to obtain a fundamentally reasonable precipitation behavior through simulations. A concerning fact can be the assumptions made and the parameters chosen in the simulations to bridge the gap between simulations and experimental data. Although there are some gaps between the simulations and the experiments, this is a good way to predict the probable process.

5.2 VICKERS HARDNESS

The sharp reduction in the hardness from the as-quenched state when tempered at 550ºC and 600ºC, can be attributed to the annihilation of the dislocations in the matrix [24][65][66]. At the initial stages of the tempering durations, molybdenum atoms, having low diffusivities, are still present in the solid solution with a few nuclei of the molybdenum-rich carbides in the matrix that have a negligible influence on the hardening effect at 0h of tempering. As the heating duration increases for the given tempering temperatures, more secondary precipitates nucleate and grow on the dislocations. Cementite, having a greater growth rate than other precipitates in the initial stages, due to the high mobility of carbon atom, has a considerable size by the time the temperature has reached 550ºC or 600ºC. The annihilation of dislocations and cementite growth can be a few reasons for a sudden reduction in the hardness.

At 550ºC, the formation of secondary precipitates is slower than that at 600ºC. This is because of the reduced diffusion of the substitutional elements in the matrix. The vanadium and molybdenum carbides are formed at temperatures between 500ºC and 700ºC [6][16][21][24]. But from the STEM-DF images, Figure 28 and Figure 29 and the PSD data, Table 8, it is seen that the molybdenum-rich particles are nucleating in the initial stages of tempering and the vanadium-rich particles are already present from the as-quenched state. This data prompts that the growth takes place later at increasing tempering durations when tempering at 550ºC. There is a further decrease in the hardness after 0h of tempering until 0.5h at 550ºC. Since the process is slower at this condition, the dislocation annihilation and cementite growth continue till 0.5h of tempering. For material A, the hardness increases gradually from 4h of tempering and

continues to increase until 96h. The nucleation of secondary precipitates on the dislocations has taken a steady rise in the supersaturated ferrite (martensite) matrix, leading to precipitation hardening. The fine dispersions have mainly suppressed the dislocation annihilation by pinning the dislocations.

At 600ºC, for both the materials, the hardness increases from 0h to 4h of tempering. The increase in hardness has the same explanation as that at 550ºC, only that the tempering times have changed. For material B, the hardness has stabilized with a peak at 1h up to 4h of tempering. This stability can be associated with the fine dispersions of the secondary precipitates at these conditions. But for material A, the hardness peak is at 4h where a large number of dislocations might have been prevented from recovery due to the matrix having a higher content of molybdenum that precipitated as carbides and hence the delay. There is a decrease in the hardness at 24h of tempering because of the growth of the secondary precipitates, as seen from Figure 28 and Table 9. On scrutinizing the hardness graphs thoroughly, it is understood that the sequence of actions in the materials at 550ºC is behind that at 600ºC. This means the hardness at 0.5h for 600ºC is similar to that at 1h for 550ºC and so on. The variation in hardness during tempering can thus, be related to the dislocation density, precipitation, growth of secondary carbides and cementite [6], and microstructural coarsening [65].

5.3 ELECTRON MICROSCOPY

The results obtained from the electron microscopy characterization highlights the chemical composition, the particle size, morphology, and distribution of the vanadium-rich carbides and the molybdenum-rich carbides in the matrix. The STEM-DF images in Figure 28 and Figure 29 depict that the particles are present in a broad size range. This can be observed from the PSD tabulated data, Table 7 to Table 9. The vanadium-rich carbides are roughly of similar size throughout the tempering process, indicated from the mean diameter. There is an increasing trend in the mean diameter for the molybdenum-rich carbides. This fairly suggests that the nucleation and the growth are taking place for the molybdenum-rich carbides, whereas there is not much growth witnessed for the vanadium-rich carbides. It is crucial to consider the standard deviation of the particles in the tables. This hints that there is a measurement error since the particle size has been measured manually, and not a significant number of particles have been analyzed. This error is more for the vanadium-rich carbides.

The presence of coarser vanadium-rich carbides in the as-quenched and the tempered samples with no appreciable growth could suggest that vanadium has already precipitated as vanadium carbides at high temperatures and is stabilized. From the TC result, Figure 10 and Figure 11 show that when nitrogen is present in the system, even in trace amounts, there is a stabilization of vanadium carbides for a considerable temperature range. The EDS composition histogram data, Figure 34 to Figure 37, illustrate that carbide enrichment is taking place across the tempering durations. Thus, the vanadium-rich carbides that might be stabilized by the nitrogen [57][58][59][60], get enriched by molybdenum and iron during tempering. On the other hand, there is nucleation and growth of molybdenum-rich carbides along with the enrichment by vanadium and iron. The morphology of the vanadium-rich carbides is approximately spherical and for the molybdenum-rich carbides vary from elongated, irregular, and rod-like.

5.4 COMPARISON WITH COMMERCIAL ALLOYS

The work on the model alloy tool steels is mainly done to study the precipitation of molybdenum-rich and vanadium-rich carbides in a simplified alloy system with more controlled heat treatment. The purpose of comparing the model alloys with the commercial alloys is to highlight the differences between the mechanical properties and the microstructures resulting from the similar heat treatment at 550°C and 600°C. The hardness comparison at similar conditions is shown in Figure 41.

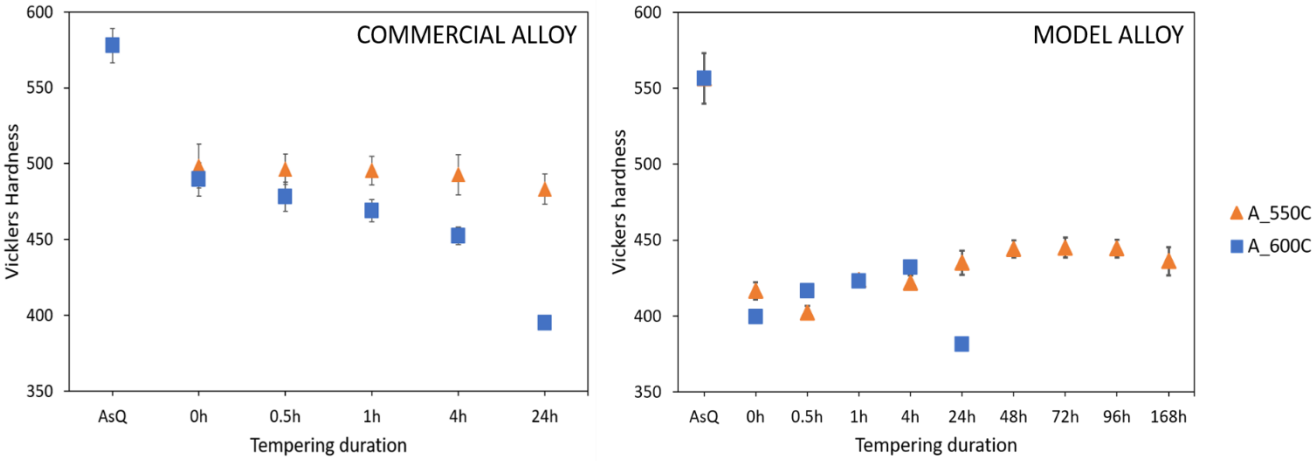

Figure 41 Hardness comparison for material A from [6] *for the commercial alloy and model alloy.*

The hardness of commercial steels is higher than that of model alloys at both the tempering temperatures, from the above figure. The addition of alloying elements like Si, Mn, Cr, and Ni to the steel provides solid solution strengthening at different temperature ranges for the commercial alloy. The combined effect of these elements contributes to the hardness stabilization by inhibiting grain growth, slowing the recovery process, pinning the dislocations by their carbides, and giving a greater supersaturation of carbon in the martensitic matrix. This helps in forming intense secondary carbides (Mo, V), thereby accelerating the precipitation hardening process [25]. The presence of silicon inhibits the conversion of ε carbide to cementite, which occurs between 200°C to 400°C [1][19]. This can be one of the reasons that the hardness did not drop drastically in commercial alloys in contrast to the model alloys, from as-quenched state to 0h. The absence of Si, Mn, Cr, and Ni in the model alloys exposes the behavior of Mo and V solely in the secondary hardening process. The lack of Si, Mn, Cr, and Ni in the model alloys could not prevent the cementite coarsening and did not aid in pinning the dislocations. The absence of small Fe-rich carbides and Nb-rich carbides in the model alloys in contrast to the commercial alloys can also contribute to the decreased hardness of the model alloys. Combined with these, and the delay in the secondary precipitation leads to the drastic decrease in hardness from as-quenched state to 0h of tempering at different tempering times in the model alloys. Moreover, grain growth, and recovery simultaneously affect the overall hardness at longer tempering times in the model alloys, and therefore, a lower hardness is witnessed.

At 550°C, in the model alloys, the secondary hardening due to fine dispersions of Mo is predominant only after 4h of tempering while for the commercial alloys it is seen from 0h of tempering. A trend in the stabilization of the hardness is seen in the commercial alloys from 0h

up to 4h, whereas in the model alloys, it is seen later from 48h to 96h of tempering at 550ºC. The stable number of large particles at these conditions for the commercial alloys could be the reason behind this relatively constant hardness [6]. For the model alloys, this stabilization can be due to a rise in the number of small-sized particles, which states that the molybdenum precipitates are effective at these conditions. Further, even distribution of these precipitates in the matrix is able to slow down the recovery and grain growth by being obstacles to the dislocation movement.

At 600ºC, the hardness decreases continuously throughout the tempering for the commercial alloys in contrast to the model alloys, where hardness increases until the peak at 4h. This is due to the growth of the small Fe-rich carbides in the matrix of the commercial alloys since the mobility of molybdenum atoms is comparatively low [6]. From [1], the drop at 24h of tempering in the commercial alloys can be attributed to the rapid coarsening of $(Fe,Cr)_7C_3$ that occurs at 600ºC in contrast to more stable carbides like Mo_2C [14]. In addition, the growth of the Fe-rich carbides causes a decrease in the number of smaller particles, and a consequent increase in the number of larger particles, lead to a drop in the hardness of the commercial alloy at 600ºC, tempered for 24h [6]. It can also be understood that at 600ºC, where the underlying processes are quicker, at initial tempering times, the grain growth, recovery, and coarsening are taking place continuously for the commercial alloy. These phenomena are controlled by Si, Mn, Cr, and Ni due to which the hardness is decreasing gradually that eventually reaches a lower hardness at 24h. On the contrary, the increasing hardness for model alloys could be due to the increased precipitation and growth of molybdenum-rich carbides in the matrix as the conditions are gradually becoming feasible. The increase in the small-sized particles in the matrix as seen in the Figure 28 for 600ºC could be the major contributing factor to this continuously increasing hardness for the model alloy. The drop in hardness at 24h of tempering for the model alloys can be attributed to the coarsening of these particles. However, it is difficult to comment on the coarsening due to limited data.

5.5 ENVIRONMENTAL, ETHICAL, AND SOCIAL ASPECTS

The Sustainable Development Goal (SDG 9) laid by the United Nations for the industries, innovation, and infrastructure targets to enhance scientific research and upgrade the technological capabilities to boost the innovation leading to the sustainable use of resources. The project on model alloy tool steels aims to study the effect of secondary precipitates on the overall hardness of the material. The techniques used to investigate these particles direct towards the systematic research to learn the behavior of the different types of carbides during tempering. The inferences drawn from the study encourage the development of the tool steels by carefully determining the characteristic features of the precipitates and the conditions that improve the properties of the steel. Thus, the research focuses on the sustainable use of resources by designing strengthened tool steels. Following the guidelines of Swerim AB to conduct the experiments in a controlled laboratory environment, safe disposal of the chemicals, and responsible consumption of the resources marks the security of the environment from exploitation. The optimal design of steel for enhancing the performance intends to reduce the cost of manufacturing. The project being a collaboration between Swerim AB and KTH, brings industry and university together, thereby building partnerships for collective progress.

6 CONCLUSIONS

- The hardness of material A is higher than material B at 550ºC and 600ºC because of higher molybdenum content in material A.

- From the hardness and STEM-EDS results, the hardness of material A at 550ºC is higher than at 600ºC for increasing tempering times, from 24h and further up to 168h.

- Comparing the hardness results of the commercial alloy and the model alloy for material A, it is interpreted that the presence of alloying elements, Si, Mn, Cr, and Ni have increased the hardness of the commercial alloy, which is greater than the model alloy at all tempering durations at 550ºC and 600ºC.

- The chemical composition data acquired from the STEM-EDS spectral analysis state that there is an enrichment of vanadium-rich carbides by iron and molybdenum and vice versa.

- The particle size of the vanadium-rich and molybdenum-rich carbides depicts that the vanadium-rich carbides are larger in size than molybdenum-rich carbides at all stages of tempering. This is because of the presence of vanadium carbides from higher temperatures that are stabilized by nitrogen. Also, at higher tempering durations, vanadium and molybdenum are soluble in each other's particles. However, it is important to remember the number of particles detected for material A that raises concern regarding the size.

- In the commercial alloys, the cementite particles were in a similar size range as the secondary carbides. This made it difficult to conclude the hardness contribution from the secondary carbides only. From the hardness, STEM-EDS, and particles size results, the hardness contribution by the finely dispersed secondary carbides in smaller size ranges, namely vanadium-rich carbides and molybdenum-rich carbides, was identified in model alloy tool steels.

- The TC-Prisma simulations show that when the dislocation density is $10^{15}m^{-2}$, the mean diameter of the molybdenum-rich carbides is very small when compared to that obtained from the experimental data. In contrast, the number density and the volume fraction seem to be promising because of the inferences gained from STEM-EDS results.

7 FUTURE RECOMMENDATIONS

The lack of characterizing all the carbides present in the matrix poses a limitation in obtaining a complete particle size distribution. With STEM, it is difficult to quantify the volume fraction less than 1%, and in this work, the volume fraction of the precipitates is lower than 1%. Further, there is an obstacle in illustrating the number density. These constraints can be eliminated using a higher resolution characterization technique such as small-angle neutron scattering (SANS) done in commercial alloys [6]. Also, diffraction studies involving Precession electron diffraction (PED) can be applied to get information about the diffraction pattern from each spot in the matrix. This is beneficial to obtain a clear picture of the different carbide types of particles in the matrix. Through this technique, a better understanding of nucleation, growth, and coarsening of the carbides can be fetched. PED can also be used for investigating the chemical composition by minimizing the risk of channeling of the electrons when compared to the EDS [67]. In the simulations, the mobility enhancement pre-factors can be included to model the precipitation calculations to obtain data close to the experimental results.

8 ACKNOWLEDGEMENTS

This work is a co-operation between Swerim AB and KTH Royal Institute of Technology in Stockholm, Sweden. The work was conducted at Swerim AB, in the spring of 2020.

This thesis wouldn't have been possible without the continuous support and guidance from a lot of people. I would first like to thank my family for their love, trust, and encouragement to pursue my studies abroad. Their faith in me has been the prime motivation for seeking education at a prestigious institution like KTH.

I am grateful to Erik Claesson, Senior Researcher, Low-Alloy Steel & Material Modeling, Swerim AB, for his constant supervision throughout this work. His support and guidance in understanding the martensitic steels, characterization, and analysis techniques have helped me to build a thorough knowledge on this topic. A big thanks to him for answering all my questions amidst the experimental and literature work. I would also like to appreciate Hans Magnusson, Group Manager, Low-Alloy Steel & Material Modeling, Swerim AB for his support in ThermoCalc software in this project.

Further, I would like to thank Peter Hedström, Professor, Department of Materials Science and Engineering, KTH, who not only gave me the opportunity to work on a very intriguing and nurturing thesis work but also guided me throughout the thesis by his feedback. The discussions over regular meetings have proved to be the backbone of this thesis work.

I would also extend my deepest gratitude to my friends, who balanced my weekends with fun-filled activities and conversations that kept me motivated throughout my thesis work.

Regards,
Jubica
Stockholm, 2020

9 REFERENCES

[1] R. A. Grange, C. R. Hribal, and L. F. Porter, “HARDNESS OF TEMPERED MARTENSITE IN CARBON AND LOW-ALLOY STEELS.,” *Met. Trans A*, 1977, doi: 10.1007/BF02646882.

[2] F. Forouzan, M. A. Guitar, E. Vuorinen, and F. Mücklich, “Effect of carbon partitioning, carbide precipitation, and grain size on brittle fracture of ultra-high-strength, low-carbon steel after welding by a quenching and partitioning process,” *Metals (Basel).*, vol. 8, no. 10, 2018, doi: 10.3390/met8100747.

[3] H. Zou and J. S. Kirkaldy, “Niobium carbide precipitate growth in a microalloyed steel,” *Can. Metall. Q.*, vol. 28, no. 2, pp. 171–177, Jan. 1989, doi: 10.1179/cmq.1989.28.2.171.

[4] O. Prat, J. García, D. Rojas, J. P. Sanhueza, and C. Camurri, “Study of nucleation, growth and coarsening of precipitates in a novel 9%Cr heat resistant steel: Experimental and modeling,” *Mater. Chem. Phys.*, vol. 143, no. 2, pp. 754–764, Jan. 2014, doi: 10.1016/j.matchemphys.2013.10.010.

[5] T. Rey, “Investigation of Microstructure and Mechanical Properties in Hot-work Tool Steels.”

[6] E. Claesson, H. Magnusson, J. Kohlbrecher, M. Thuvander, F. Lindberg, and M. Andersson, “Carbide precipitation in commercially processed tempered martensitic steels : Complete characterization using Small- Angle Scattering , Electron Microscopy and Atom Probe,” pp. 1–21.

[7] S. S. Yugai, L. M. Kleiner, A. A. Shatsov, and N. N. Mitrokhovich, “STRUCTURAL STEELS STRUCTURAL HEREDITY IN LOW-CARBON MARTENSITIC STEELS,” 2004.

[8] G. A. Roberts, G. Krauss, and R. Kennedy, “Principles of tool steel heat treatment,” *Tool Steels*, p. 86, 1998.

[9] G. B. Olson, “Introduction: Martensite in Perspective,” in *MARTENSITE-A Tribute to Morris Cohen*, W. S. Olson, G.B., Owen, Ed. ASM International, 1992, 1992, p. 3.

[10] B. C. Muddle and J. F. Nie, “Martensite,” *Encycl. Mater. Sci. Technol.*, pp. 5189–5193, Jan. 2001, doi: 10.1016/B0-08-043152-6/00901-3.

[11] R. Roberts, George; Krauss, George; Kennedy, “Tool Steel Alloy Design,” in *Tool Steels*, 5th ed., R. Roberts, George; Krauss, George; Kennedy, Ed. ASM International, 1998.

[12] K. E. Porter, D. A. ; Easterling, “Diffusionless Transformations,” in *Phase Transformations in Metals and Alloys*, 2nd ed., pp. 388–420.

[13] C. R. Hutchinson and Y. Brechet, “Solute Drag,” in *Thermodynamics, Microstructures and Plasticity*, Springer Netherlands, 2003, pp. 155–166.

[14] G. R. Speich and W. C. Leslie, “Tempering of Steel.”

[15] H. K. D. H. Bhadeshia and S. R. Honeycombe, “The Tempering of Martensite,” in *Steels*, 2006.

[16] K. A. Speich, G.R., Taylor, “Tempering of Ferrous Martensites,” in *MARTENSITE: A tribute to Morris Cohen*, G.B. Olson and W.S. Owen, Ed. ASM International, 1992, 1992, pp. 250–257.

[17] G. Krauss, “5 Tempering of martensite in carbon steels.”

[18] J. S, “Alloying Elements: Distribution and Effects | Metallurgy.” [Online]. Available:

https://www.engineeringenotes.com/metallurgy/alloying-elements/alloying-elements-distribution-and-effects-metallurgy/25701. [Accessed: 24-Sep-2020].

[19] J.-C. Eun, "Types and Requirements of Materials and Corrosion," in *Handbook of Engineering Practice of Materials and Corrosion*, Springer, pp. 122–123.

[20] D. V Doane, "Application of Hardenability Concepts in Heat Treatment of Steel," *J. Heat Treat.*, vol. 1, 1979.

[21] M. Maalekian and M. Maalekian, "Christian Doppler Laboratory for Early Stages of Precipitation The Effects of Alloying Elements on Steels (I)," 2007.

[22] S. Yamasaki and H. K. D. H. Bhadeshia, "Modelling Precipitation of Carbides in Martensitic Steels."

[23] B. Kim, E. Boucard, T. Sourmail, D. San Martín, N. Gey, and P. E. J. Rivera-Díaz-Del-Castillo, "The influence of silicon in tempered martensite: Understanding the microstructure-properties relationship in 0.5-0.6 wt.% C steels," *Acta Mater.*, vol. 68, pp. 169–178, Apr. 2014, doi: 10.1016/j.actamat.2014.01.039.

[24] H. Bhadeshia and R. Honeycombe, "Tempering of Martensite," in *Steels: Microstructure and Properties*, Elsevier, 2017, pp. 237–270.

[25] P. Michaud *et al.*, "The effect of the addition of alloying elements on carbide precipitation and mechanical properties in 5% chromium martensitic steels," *Acta Mater.*, vol. 55, no. 14, pp. 4877–4889, 2007, doi: 10.1016/j.actamat.2007.05.004ï.

[26] K. E. Porter, D. A. ; Easterling, "Diffusional Transformation in Solids," in *Phase Transformations in Metals and Alloys*, 2nd ed., K. E. Porter, D. A. ; Easterling, Ed. pp. 338–344.

[27] R. Bhadeshia, Harry; Honeycombe, "The heat treatment of steels: hardenability," in *Steels: Microstructure and Properties*, 3rd ed., R. Bhadeshia, Harry; Honeycombe, Ed. Elsevier, 2006, pp. 176–179.

[28] H. Mohrbacher, "Property optimization in as-quenched martensitic steel by molybdenum and niobium alloying," *Metals*, vol. 8, no. 4. MDPI AG, 01-Apr-2018, doi: 10.3390/met8040234.

[29] G. Krauss, "Tempering of steel," in *Steels : Processing, Structure, and Performance.*, 2nd ed., ASM International, 2015.

[30] R. Bhadeshia, Harshad;Honeycombe, "Formation of martensite," in *Steels:Microstructures and properties*, 4th ed., R. Bhadeshia, Harshad;Honeycombe, Ed. Elsevier, 2006, pp. 120–122.

[31] "https://en.wikipedia.org/wiki/Transmission_electron_microscopy#Scanning_TEM." .

[32] S. G. Wolf, E. Shimoni, and M. Elbaum, "Cellular Imaging Insights," no. January, 2018, doi: 10.1007/978-3-319-68997-5.

[33] D. Alexander, "Scanning TEM (STEM): Imaging & Resolution 1 Duncan Alexander EPFL-CIME."

[34] "Structural Characterization of Quantum Dots."

[35] N. Mehrban and J. Bowen, "Monitoring biomineralization of biomaterials in vivo," *Monit. Eval. Biomater. their Perform. Vivo*, pp. 81–110, Jan. 2017, doi: 10.1016/B978-0-08-100603-0.00005-5.

[36] “Plant-Mediated Green Synthesis of Nanostructures: Mechanisms, Characterization, and Applications,” *Interface Sci. Technol.*, vol. 28, pp. 199–322, Jan. 2019, doi: 10.1016/B978-0-12-813586-0.00006-7.

[37] O. D. Neikov, S. S. Naboychenko, N. A. Yefimov, O. D. Neikov, and N. A. Yefimov, “Powder Characterization and Testing,” *Handb. Non-Ferrous Met. Powders*, pp. 3–62, Jan. 2019, doi: 10.1016/B978-0-08-100543-9.00001-4.

[38] D. Brabazon and A. Raffer, “Advanced characterization techniques for nanostructures,” *Emerg. Nanotechnologies Manuf.*, pp. 53–85, Jan. 2015, doi: 10.1016/B978-0-323-28990-0.00003-8.

[39] J. Bergström and J. Bergström, “Experimental Characterization Techniques,” *Mech. Solid Polym.*, pp. 19–114, Jan. 2015, doi: 10.1016/B978-0-323-31150-2.00002-9.

[40] A. F. Ismail, K. C. Khulbe, T. Matsuura, A. F. Ismail, K. C. Khulbe, and T. Matsuura, “RO Membrane Characterization,” *Reverse Osmosis*, pp. 57–90, Jan. 2019, doi: 10.1016/B978-0-12-811468-1.00003-7.

[41] O. G. Raabe, “PARTICLE SIZE ANALYSIS UTILIZING GROUPED DATA AND THE LOG-NORMAL DISTRIBUTION*,” Pergamon Press, 1971.

[42] “Probability Density Function.” [Online]. Available: https://en.wikipedia.org/wiki/Probability_density_function.

[43] M. A. Vaz, M.fatima ; Fortes, “GRAIN SIZE DISTRIBUTION: THE LOG-NORMAL AND THE GAMMA DISTRIBUTION FUNCTIONS,” 1988.

[44] M. LIMPERT, ECKHARD ; STAHEL, WERNER A.; ABBT, “Log-normal Distributions across the Sciences: Keys and Clues,” 2001.

[45] W. A. Limpert, Eckhard ; Stahe, “The log-normal distribution,” 2017, doi: 10.1371/journal.pone.002140.

[46] “Particle Size, Size Distributions and Shape Contents,” doi: 10.1007/978-1-4020-9015-8_2.

[47] Thermo-Calc AB, “The Precipitation Module (TC-PRISMA) User Guide,” 2020.

[48] J. P. Sanhueza *et al.*, “Precipitation kinetics in a 10.5%Cr heat resistant steel: Experimental results and simulation by TC-PRISMA/DICTRA,” *Mater. Chem. Phys.*, vol. 200, pp. 342–353, Oct. 2017, doi: 10.1016/j.matchemphys.2017.07.083.

[49] Z. Hou, P. Hedström, Q. Chen, Y. Xu, D. Wu, and J. Odqvist, “Quantitative modeling and experimental verification of carbide precipitation in a martensitic Fe-0.16 wt%C-4.0 wt%Cr alloy,” *Calphad Comput. Coupling Phase Diagrams Thermochem.*, vol. 53, pp. 39–48, Jun. 2016, doi: 10.1016/j.calphad.2016.03.001.

[50] J. H. Jang, C.-H. Lee, Y.-U. Heo, and D.-W. Suh, “Stability of (Ti, M)C (M = Nb, V, Mo and W) carbide in steels using first-principles calculations,” *Acta Mater.*, vol. 60, no. 1, pp. 208–217, Jan. 2012, doi: 10.1016/J.ACTAMAT.2011.09.051.

[51] S. Yamasaki and H. K. D. H. Bhadeshia, “Modelling and characterisation of V4C3 precipitation and cementite dissolution during tempering of Fe - C - V martensitic steel,” *Mater. Sci. Technol.*, vol. 19, no. 10, pp. 1335–1343, Oct. 2003, doi: 10.1179/026708303225005971.

[52] W. S. Jung and S. H. Chung, “Ab initio calculation of interfacial energies between transition metal carbides and fcc iron,” *Model. Simul. Mater. Sci. Eng.*, vol. 18, no. 7, Oct. 2010, doi: 10.1088/0965-0393/18/7/075008.

[53] N. Fujita and H. K. D. H. Bhadeshia, “Precipitation of molybdenum carbide in steel: Multicomponent diffusion and multicomponent capillary effects,” *Mater. Sci. Technol.*, vol. 15, no. 6, pp. 627–634, 1999, doi: 10.1179/026708399101506364.

[54] S. Lu, J. Ågren, and L. Vitos, “Ab initio study of energetics and structures of heterophase interfaces: From coherent to semicoherent interfaces,” *Acta Mater.*, vol. 156, pp. 20–30, Sep. 2018, doi: 10.1016/j.actamat.2018.06.030.

[55] “Distribution fitting.” [Online]. Available: https://www.spcforexcel.com/knowledge/basic-statistics/distribution-fitting.

[56] “Deciding which distribution fits your data best.” [Online]. Available: https://www.spcforexcel.com/knowledge/basic-statistics/deciding-which-distribution-fits-your-data-best.

[57] J. Gu, J. Li, R. Chang, and L. Li, “Comprehensive effect of nitrogen on Cr-Mo-V hot-working die steel with enhanced strength and toughness,” *Mater. Sci. Eng. A*, vol. 766, no. September, p. 138386, 2019, doi: 10.1016/j.msea.2019.138386.

[58] N. K. Balliger and R. W. K. Honeycombe, “The effect of nitrogen on precipitation and transformation kinetics in vanadium steels,” *Metall. Trans. A*, vol. 11, no. 3, pp. 421–429, 1980, doi: 10.1007/BF02654566.

[59] V. Ollilainen, W. Kasprzak, and L. Holappa, “The effect of silicon, vanadium and nitrogen on the microstructure and hardness of air cooled medium carbon low alloy steels,” *J. Mater. Process. Technol.*, vol. 134, no. 3, pp. 405–412, 2003, doi: 10.1016/S0924-0136(02)01131-7.

[60] M. Hirano and N. Kawai, “Effect of Nitrogen on High Speed Steels.,” *Met. Powder Rep.*, vol. 41, no. 7, pp. 527–531, 1986, doi: 10.19080/JOJMS.2019.05.555667.

[61] T. Zhou, R. Prasath Babu, J. Odqvist, H. Yu, and P. Hedström, “Quantitative electron microscopy and physically based modelling of Cu precipitation in precipitation-hardening martensitic stainless steel 15-5 PH,” *Mater. Des.*, vol. 143, pp. 141–149, 2018, doi: 10.1016/j.matdes.2018.01.049.

[62] J. Svoboda, F. D. Fischer, P. Fratzl, and E. Kozeschnik, “Modelling of kinetics in multi-component multi-phase systems with spherical precipitates I: Theory,” *Mater. Sci. Eng. A*, vol. 385, no. 1–2, pp. 166–174, 2004, doi: 10.1016/j.msea.2004.06.018.

[63] B. Sonderegger and E. Kozeschnik, “Generalized nearest-neighbor broken-bond analysis of randomly oriented coherent interfaces in multicomponent Fcc and Bcc structures,” *Metall. Mater. Trans. A Phys. Metall. Mater. Sci.*, vol. 40, no. 3, pp. 499–510, 2009, doi: 10.1007/s11661-008-9752-6.

[64] A. A. H. Ameri, N. N. Elewa, M. Ashraf, and J. P. Escobedo-Diaz, “General methodology to estimate the dislocation density from microhardness measurements,” *Mater. Charact.*, vol. 131, no. June, pp. 324–330, 2017, doi: 10.1016/j.matchar.2017.06.031.

[65] Z. Hou, R. P. Babu, P. Hedström, and J. Odqvist, “Microstructure evolution during tempering of martensitic Fe–C–Cr alloys at 700 °C,” *J. Mater. Sci.*, vol. 53, no. 9, pp. 6939–6950, 2018, doi: 10.1007/s10853-018-2036-7.

[66] F. H. Samuel and A. A. Hussein, “A comparative study of tempering in steel,” *Mater. Sci. Eng.*, vol. 58, no. 1, pp. 113–120, 1983, doi: 10.1016/0025-5416(83)90142-8.

[67] “Precession electron diffraction.” [Online]. Available: https://en.wikipedia.org/wiki/Precession_electron_diffraction.